FINAL REPORT

DE-FC07-07ID14825

6/01/07-09/30/11

Establishing a Scientific Basis for Optimizing Compositions, Processes Paths and Fabrication Methods for Nanostructured Ferritic Alloys for Use in Advanced Fission Energy Systems

Principal Investigator: G. Robert Odette, Professor

University of California at Santa Barbara

Santa Barbara CA 93106

January 30, 2012

Table of Contents

1.0 INTRODUCTION AND SUMMARY **6**
1.1 PROGRAM OBJECTIVES AND STRUCTURE 6
1.2 BACKGROUND AND SUMMARY 8

2.0 MATERIALS AND METHODS IN TASKS 2, 3 AND 4 ..... **12**
2.1 BEST PRACTICE NFA HEAT 12
2.1.1 Atomized powder batches *13*
2.1.2 Powder milling *15*
2.1.3 Powder annealing and consolidation *17*
2.2 COMPOSITION AND PROCESSING VARIATIONS 20
2.3 SOLID STATE JOINING 22
2.4 TARGET OF OPPORTUNITY IRRADIATIONS 23

3.0 SUMMARY OF THE CHARACTERIZATION TECHNIQUES **26**
3.1 SMALL ANGLE NEUTRON SCATTERING 26
3.2 ATOM PROBE TOMOGRAPHY 29
3.3 TRANSMISSION ELECTRON MICROSCOPY 33
3.4 OTHER TECHNIQUES 33

4.0 SUMMARY OF RESULTS: DEVELOPING A LARGER BEST PRACTICE HEAT OF 14YWT, NFA OPTIMIZATION AND NF CHARACTERIZATION **35**
4.1 DEVELOPING A LARGER BEST PRACTICE HEAT OF 14YWT 35
4.1.1 Composition and solute distribution and microstructure *35*
4.1.1.1 EPMA and Chemical Analysis 35
4.1.1.2 TEM and APT characterization 39
4.1.1.3 Grain structure 48
4.1.2 NF characterization *51*
4.1.2.1 SANS 52
4.1.2.2 TEM 58
4.1.2.3 APT 63
4.1.2.4 Oxygen effects 70
4.1.3 Mechanical testing *77*
4.2 A SYSTEMATIC STUDY OF THE EFFECTS OF Y AND TI VARIATIONS 78
4.2.1 Oxygen and Nitrogen content *78*
4.2.2 SANS *79*
4.2.3 APT *81*
4.3 FRICTION STIR WELDING 82

5.0 SUMMARY AND CONCLUSIONS **89**
ACKNOWLEDGMENTS *93*
REFERENCES *94*

List of Figures

Figure 2.1. 32 mm stainless steel HIP can a) before; b) after HIPing; c) example of HIPing multiple powders in a single can. 20

Figure 4.1. EPMA analysis of the Y concentration in a) Ar as-atomized powder L2311S; b) after 10 h SPEX milling. 36

Figure 4.2. Variation on the O and N content in Ar atomized L2311M powders as a function of milling time. 37

Figure 4.3. Bright field image and EDX spectrum of an elongated Y-rich precipitate in He atomized L2313S powder. 40

Figure 4.4. Y precipitates in Ar atomized (L2311S) powder. 41

Figure 4.5. a) 10 nm thick by 20 nm X 40 nm atom maps showing uniform distribution of Fe, Cr, W, and Ti; b) mass spectrum showing no Y. 42

Figure 4.6. Atom maps of 40 h as-milled Ar atomized L2311M powder showing solute dissolution with some enrichment on boundaries, and associations of YO, TiO, and WN and TiN ions. The reconstruction volume is 10 nm x 20 nm x 40 nm. 43

Figure 4.7. Mass spectrum of L2311M powder attritor milled for 40 h showing TiN and WN peaks. ... 44

Figure 4.8. A nitrogen iso-density surface (1.35 solute atom/nm^3) for a large nitride precipitate along with TiN and Al ions showing an associated aluminum oxide precipitate. 45

Figure 4.9. BF TEM images showing large Ti-O precipitates in a) OW1 and b) OW2. 46

Figure 4.10. Composition and m/c spectrum of milled L2311S powder using improved attritor milling procedure. 47

Figure 4.11. Atom maps showing solute segregation in milled L2311S powder using improved attritor milling procedure. 48

Figure 4.12. Grain structure of Ar atomized and annealed L2311M powder with attritor milling times of: a) 1 h; b) 5 h; and c) 20 h. 49

Figure 4.13. Optical micrographs of etched OWH (a); OWL (b); and OWI (c). 50

Figure 4.14. BSE SEM image of extruded alloy PM2. 51

Figure 4.15. Example graph comparing Ar as-atomized powder with baseline Fe14Cr0.3W0.4Ti powder without Y. 52

Figure 4.16. SANS 45° scattering curves comparing the Ar, Ar/O and He atomized, SPEX milled and annealed powders (L2311S, L2312S and L2313S). 53

Figure 4.17. a) SANS 45° scattering curves comparing the Ar/O atomized, attritor milled and annealed powders (L2312M) for milling from 1 to 40 h and b) a comparison of the size, number density, and volume fraction of select 14YWT powders and alloys. 55

Figure 4.18. SANS 45° scattering curves comparing the OW1, OW3, and OW4 alloys. 56

Figure 4.19. Bright field TEM images showing some large Y rich precipitates and numerous NFs in 40 h attritor milled and annealed a) Ar (L2311M); and b) Ar/O (L2312M) powders; c) L237BS milled and annealed powder with larger precipitates; and d) L2311M powder milled with FeO and annealed showing high density of small NFs. 59

Figure 4.20. Low magnification TEM images show grain structure in a) OW1 and b) OW2, respectively. Higher magnification TEM images show NFs in the large grains for both c) OW1 and d) OW2. ... 61

FIGURE 4.21. ALLOY OW2 A) BRIGHT FIELD TEM IMAGE OF NFS IN EXTRACTION REPLICA SAMPLE; AND B) HRTEM IMAGE OF SINGLE NF < 5 NM IN DIAMETER. 62

FIGURE 4.22. BRIGHT FIELD TEM IMAGES OF EXTRUDED AND CROSS-ROLLED PM2 ALLOY. 63

FIGURE 4.23. AN APT ATOM MAP RECONSTRUCTION OF A SMALL GRAIN REGION IN THE 10 H SPEX MILLED AND ANNEALED AR ATOMIZED POWDER (L2311S) SHOWING PHOSPHORUS SEGREGATION TO GRAIN BOUNDARIES AND Y-TI-O ISO-DENSITY SURFACES (0.9 ATOM/NM^3) FOR THE NFS. 64

FIGURE 4.24. A) A DUAL-BEAM FIB IMAGE OF BIMODAL GRAIN DISTRIBUTION IN A 10H SPEX MILLED AR ATOMIZED AND ANNEALED L2311S POWDER SHOWING THE PT MASKED FIB LIFT-OUT AREA; B) Y-TI-O ISO-DENSITY SURFACES (2 ATOM/NM^3) IN BLUE SHOWING NFS IN LARGE GRAIN REGION. 65

FIGURE 4.25. AN APT RECONSTRUCTION OF A VOLUME IN THE OW1 ALLOY. C ATOMS (GREY) ARE SEGREGATED AT A GRAIN BOUNDARY. ISO-CONCENTRATION SURFACES (11%) FOR TIN IONS ARE SHOWN IN GREEN AND FOR Y+YO IONS (1%) FROM THE NFS ARE SHOWN IN BLUE. 67

FIGURE 4.26. AN APT RECONSTRUCTION OF A VOLUME OF OW2 ANALYZED BY APT. THE NFS ARE SHOWN TI BY TIO AND YO ISO-COMPOSITION SURFACES (0.9 AT%). 68

FIGURE 4.27. COMPARISON OF THE NUMBER DENSITY AND THE AVERAGE DIAMETER OF NFS IN THE AR ATOMIZED, 40 H ATTRITOR MILLED AND ANNEALED POWDER (L2311M) AND OW1 AND OW2 ALLOYS. 69

FIGURE 4.28. COMPARISON OF THE SIZE DISTRIBUTION OF NFS IN THE L2311S POWDER, OW1 AND OW2 MEASURED BY APT. 70

FIGURE 4.29. A) AN APT RECONSTRUCTION OF A VOLUME IN THE OWL ALLOY SHOWING A LOWER DENSITY OF LARGER NFS COMPARED TO THE RESULTS FOR THE PRELIMINARY BATCHES OF POWDERS (Y ISOCONCENTRAITION = 0.5%); B) BRIGHT FIELD TEM MICROGRAPHS SHOWING NFS IN OWL ALLOY. 71

FIGURE 4.30. TEM MICROGRAPHS OF THE NFS IN OWH (A); OWL (B); AND OWI (C). 73

FIGURE 4.31. SIZE DISTRIBUTIONS OF THE NFS IN OWH, OWL AND OWI MEASURED BY BF TEM. 73

FIGURE 4.32. TWENTY NM THICK ATOM MAPS WITH CR IONS AND Y-TI-O ISOCONCENTRATION SURFACES (4.0%) FOR (A) OWH, (B) OWL, AND (C) OWI. 74

FIGURE 4.33. A) VOLUME FRACTION (F_V) AND B) NUMBER DENSITY (N) VERSUS Y_2O_3 FOR EACH TI/Y RATIO. 80

FIGURE 4.34. <R> VERSUS Y_2O_3 FOR EACH TI/Y RATIO. 81

FIGURE 4.35. A) AN APT 3-D RECONSTRUCTION OF A VOLUME OF THE FSW MA957 SHOWING THE ISOCONCENTRATION SURFACES (1 AT.% TIO AND YO) TO IDENTIFY THE NFS. ARROWS INDICATE A BOUNDARY. A BLOW-UP OF THE TIO, YO+Y AND O ATOMS FOR A LARGER FEATURE IS ALSO SHOWN; B) FSW-A SAMPLE WITH LOWER NUMBER DENSITY OF NFS. 85

FIGURE 4.36. THE APT NF SIZE DISTRIBUTIONS FOR THE FSW AND FSW-A MA957. 87

FIGURE 4.37. A BRIGHT FIELD TEM IMAGE OF CRYSTALLINE $Y_2TI_20_7$ OXIDES IN THE FSW-A DOWN TO APPROXIMATELY 1 NM. 88

List of Tables

TABLE 2.1. COMPOSITION AND SIZES OF ATOMIZED POWDERS FROM ATI POWDER METALS. 14

TABLE 2.2. ANALYSIS SUMMARY ON AS-ATOMIZED POWDERS. 15

TABLE 2.3. ANALYSIS SUMMARY ON MILLED POWDERS. 17

TABLE 2.4. ANALYSIS SUMMARY ON MILLED AND ANNEALED POWDERS. 18

TABLE 2.5. ANALYSIS SUMMARY ON CONSOLIDATED ALLOYS. 19

TABLE 2.6. MILLING MATRIX SHOWING TI WT.% FOR CORRESPONDING Y_2O_3 AND TI:Y RATIO. 21

TABLE 2.7: MA957 NOMINAL COMPOSITION IN WT. %. 24

TABLE 2.8. TARGET OF OPPORTUNITY IRRADIATIONS. 25

TABLE 4.1. INTERSTITIAL COMPOSITION IN AR ATOMIZED POWDER AFTER MILLING FOR 40 H COMPARING TWO MILLING PROCEDURES. 38

TABLE 4.2. O AND N CONTENT (WT.%) FOR OW1, OW2, OW3, AND OW4 39

TABLE 4.3. COMPOSITION COMPARISON BETWEEN APT AND CHEMICAL ANALYSIS SUPPLIED BY ATI POWDER METALS OF AS-ATOMIZED POWDER (L2311S). 41

TABLE 4.4. COMPOSITION OF TWO LARGE TI-N AND ONE ASSOCIATED AL-O RICH PRECIPITATES. 46

TABLE 4.5. COMPOSITION OF FIVE LARGE TI-SI-O RICH PRECIPITATES IN OW1 AND OW2. 46

TABLE 4.6. SUMMARY OF THE SANS RESULTS. 57

TABLE 4.7. AVERAGE DIAMETER, NUMBER DENSITY, AND Y/TI RATIOS OF 14YWT ANNEALED POWDERS. 60

TABLE 4.8. THE <D>, N, F_V AND Y/TI RATIOS OF 14YWT CONSOLIDATED ALLOYS. 62

TABLE 4.9. THE AVERAGE APT COMPOSITION OF THE ATTRITOR MILLED AND ANNEALED L2311M POWDER. 66

TABLE 4.10. THE AVERAGE APT COMPOSITION OF THE NFS IN THE 40 H ATTRITOR MILLED AND ANNEALED L2311M POWDER. 66

TABLE 4.11. THE APT COMPOSITIONS OF TWO VOLUMES FROM OW1 ALLOY 67

TABLE 4.12. THE AVERAGE APT NF COMPOSITION IN THE OW1 ALLOY. 68

TABLE 4.13. THE AVERAGE APT COMPOSITION FOR THREE VOLUMES IN THE OW2 ALLOY. 68

TABLE 4.14. THE AVERAGE APT NF COMPOSITION IN THE OW2 ALLOY. 69

TABLE 4.15. O AND N CONTENT (WT.%) FOR OWL, OWI, AND OWH ALLOYS 72

TABLE 4.16. THE AVERAGE APT NF COMPOSITION IN THE OWH, OWI AND OWL ALLOYS. 74

TABLE 4.17. SUMMARY OF THE OW-ALLOY CHARACTERISTICS MEASURED IN THIS STUDY 76

TABLE 4.18. O AND N COMPARISON OF SELECT SPEX MILLED POWDERS 79

TABLE 4.19. NF COMPOSITION COMPARISON BETWEEN POWDERS WITH DIFFERENT TI/Y RATIOS. 82

TABLE 4.20. NUMBER DENSITY AND AVERAGE DIAMETER OF NFS IN THE MA957 FSW BEFORE AND AFTER ANNEALING AND IN THE AE METAL. 86

TABLE 5.1. SUMMARY OF THE CONSOLIDATED ALLOY CHARACTERISTICS MEASURED IN THIS STUDY 91

1.0 Introduction and Summary

1.1 Program objectives and structure

The broad objective of this NEUP was to further develop a class of 12-15Cr ferritic stainless steels that are dispersion strengthened and made radiation tolerant by an ultrahigh density on Y-Ti-O nanofeatures (NFs) in the size range of less than 5 nm [1,2]. We call these potentially transformable materials nanostructured ferritic alloys (NFAs) to distinguish them from oxide dispersion strengthened (ODS) steels, like PM 2000, that contain coarser and less stable oxide features, although the names are essentially interchangeable. The NEUP originally had 5 tasks:

Task 1: Deformation Processing Database

Task 2: Solid State Joining

Task 3: Alternative Alloys and Alloy Optimization

Task 4:Identification and Optimization of the Nanofeatures

Task 5: Other Miscellaneous Best Effort Tasks

However, soon after the program began in 2007 we were invited to join a consortium of institutions, led by Stuart Maloy at Los Alamos National Laboratory (LANL), to develop a new larger "best practice" heat of NFA. The consortium consists of LANL, UC Santa Barbara (UCSB), UC Berkeley (UCB), Oak Ridge National Laboratory (ORNL), South Dakota School of Mines (SDSM) and ATI Powder Metals (ATI). It was found that the moderate amount of MA957 available at that time was insufficient to support the proposed deformation processing research and the alloy also lacked sufficient ductility due to impurity Al_2O_3 stringers. Thus a decision was made to defer Task 1 until the new heat was available. This allowed UCSB to lead the characterization effort in the

consortium as well as to collaborate with ORNL in the processing design and implementation. UCB contributed to the milling activity, while SDSM led the solid sate joining task. The main focus of LANL during the period of this NEUP was program management and coordination, limited deformation processing studies on MA957 and model alloy heats of ion irradiations and texture measurements. Because of the focus on developing the processing route for the new, larger heat NFA, part of the work on Task 2 was also deferred and redirected. The solid state joining effort in the consortium was led by SDSM and UCSB assisted them on that work. The contributions of UCB have primarily been ball milling for producing small developmental batches of 14YWT. ATI provided the atomized powders. With this organizational structure in place the UCSB effort was primarily directed to Tasks 3 and 4, and the combination of our NEUP and some subcontract funding from LANL and support from our DOE Fusion Materials Program, allowed us to greatly exceed the original objectives of Tasks 3 and 4, while enabling the consortium to make significant progress on all aspects of its processing research. These efforts have culminated in developing procedures and specifications for producing a new best practice larger heat of 14YWT, which is currently being processed. Task 5 has been pursued on a best effort basis involving the NFA specimens in several irradiation experiments.

This Final Report is organized as follows. We begin with an introduction and summary of the work. A materials and methods section follows with a description of each material characterization technique used. We then summarize the combined optimized alloy development and NF characterization efforts in Tasks 3 and 4. Finally, the results involving activities in Tasks 2 and 5 are briefly described.

1.2 Background and summary

NFAs are typically processed by ball milling pre-alloyed rapidly solidified powders and yttria (Y_2O_3) powders [1,2]. Proper milling effectively dissolves the Ti, Y and O solutes that then precipitate as NFs during hot consolidation. Powder consolidation is followed by a series of deformation processing treatments. The current study examines an alternative processing path, involving rapid solidification by gas atomization of Fe, 14% Cr, 3% W, and 0.4% Ti powders that are also pre-alloyed with 0.2% Y (14YWT), where the compositions are in wt.%. The focus is on exploring the possibility of minimizing, or even eliminating, the milling time, as well as producing alloys with more homogeneous distributions of NFs and a more uniform, fine grain size. Three atomization environments were explored: Ar, Ar plus O (Ar/O) and He. The powders were sieved into three mesh sizes: -35+100 (149 μm to 500μm), -100+35 (44 μm to 149 μm) and -325 (< 44 μm). Further details on the powder atomization are presented in section 2.1.1.

The foundation of this research is characterization of powders and alloys through each processing step: powder production by gas atomization; powder milling; and powder hot consolidation by hot isostatic pressing (HIPing) or hot extrusion. Annealing the powders with a temperature cycle mimicking that for hot consolidation is a useful expedient that produces equivalent NFs and other microstructural characteristics compared to fully densified alloys.

The characterization studies of the preliminary batches of powders described here include various combinations of: a) bulk chemistry (at Luvak, Inc. and ATI Powder Metals); b) electron probe microanalysis (EPMA); c) atom probe tomography (APT); d) small angle neutron scattering (SANS); e) various types of scanning and transmission

electron microscopy (SEM and TEM) including energy dispersive x-ray spectroscopy (EDX); f) microhardness testing; and limited tensile, creep and fracture testing. The microstructural-microanalytical characterization methods were variously used to characterize the material in the as-atomized, ball milled, ball milled and annealed, and HIPed and hot extruded consolidated conditions.

The bulk chemistry measurements show that preliminary batches of gas-atomized powders could be produced within specified composition ranges. However, EPMA and TEM showed that the Y is heterogeneously distributed and phase separated, but TEM, SANS and APT show that attritor milling for 20 to 40 h sufficiently mixes the Y. Notably, however, effective mixing does not occur at lower milling times. The initial milling procedures in this study added a significant quantity of O as well as contaminant N to the powders. TEM, SANS and APT showed that subsequent powder annealing treatments, typically at 1150°C, result in the precipitation of a high density of NFs. All the annealed powder variants and HIP consolidated alloys had a bimodal distribution of grain sizes; however, APT and TEM show the presence of NFs in both large and small grains. In contrast, alloys extruded at lower temperature of 850°C contain a unimodal distribution of fine grains.

These preliminary studies led to the atomization of a larger ≈ 58 kg batch of powder in Ar. Improved milling procedures at UCB applied to these powders led to the effective elimination of the impurity N, but also resulted in lower O content that was insufficient to produce Y-Ti-O NFs in the size range below about 3 nm. TEM showed that the low O resulted in fewer and larger oxide phases that are more highly enriched in Y, resulting in low Vicker's hardness values ≈ 250 kg/mm^2 in powders annealed at 1150°C. This

compares to hardness value of ≈ 443 kg/mm^2 in an alloy consolidated from the preliminary powders with higher O content.

In order to overcome the problem of O deficiency in the low impurity powders, ORNL added FeO during 40 h attritor milling to increase the O content to a nominal value of 0.135%. The annealed powder and corresponding 1150°C HIP and 850°C extrusion consolidated alloys showed a very uniform distribution of fine scale NFs. The HIP consolidated alloy had promising high temperature creep strength, but low toughness and a high ductile to brittle transmission temperature (DBTT). An extruded and cross-rolled alloy processed at 850ºC, however, exhibited a lower DBTT. While the creep properties of the extruded and cross-rolled extrusion are still under investigation, very preliminary results suggest the alloy is strong but may have limited ductility.

Based on this large body of preliminary research a set of specification was developed for milling a large batch of ATI powders with FeO under a contract to the Zoz GmbH in Germany. The new milled powders will be prepared in early 2012, and after verification of their compositions and Y distribution the powders will be consolidated by extrusion and HIPing.

We also investigated the effects of Ti and Y content on the NFs in several alloys that were produced from conventionally milled powders that varied Y_2O_3 from 0.2 to 0.5 wt.% while maintaining Ti/Y ratios of 1.6, 2.4, and 3.1. SANS showed the volume fraction and number density of the NFs increases with Y and to a lesser extent Ti. Notably, the NF size and composition are relatively independent of the alloy Y and Ti content, except at the lowest Y_2O_3 concentration of 0.2 wt.%.

An APT characterization of MA957 joined by friction stir welding (FSW) showed that this solid sate joining procedure had only a modest effect on the NF number density (N) and average diameter (<d>) compared to an as extruded sample. Annealing at 1150ºC for 3 h following FSW reduces N, consistent with a significant reduction in hardness. FSW appears to rearrange the NFs, which become highly aligned with sub-boundary and dislocation structures to an extent that are not observed in the as extruded case. The aligned NF structures are less apparent, but seem to persist after post weld annealing.

Several NFA materials, including MA957 and various 14YWT alloys, have been included in irradiation experiments. These experiments have been performed or are currently in play at numerous facilities including the Advanced Test Reactor (ATR), the JOYO sodium cooled fast reactor, the High Flux Isotope Reactor (HFIR), and the SINQ spallation neutron source for the SINQ Target Irradiation Program (STIP).

2.0 Materials and Methods in Tasks 2, 3 and 4

As described in the introduction, the major focus of our NERI program was on: a) exploring an alternative NFA processing path, involving the addition of Y during atomization; and b) developing a larger "best practice" heat of 14YWT. We also characterized the effects of variations in the 14YWT alloy O, Ti and Y contents on the NFs and the effects friction stir welding has on the NFs in MA957.

ATI Powder Metals (formerly Crucible Research, Pittsburgh, PA) produced the pre-alloyed powders. Milling was carried out at UCSB, ORNL and UCB. The powders were consolidated by UCSB (HIPing) and ORNL (extrusion). Characterization of the powders and alloys was performed primarily at UCSB and to a lesser extent at ORNL.

Our research employed a full suite of experimental tools to characterize the NFs and see how they vary with alloy composition and processing paths. The scope of the 14YWT "best practice" study was broad, focusing on the effectiveness of the new processing path in producing homogeneous NF distributions, high dislocation densities and fine scale grain structures. The corresponding effects on the mechanical properties were also characterized to a limited extent.

2.1 Best practice NFA heat

The collaborative effort to produce a "best practice" NFA heat first aimed to reduce or eliminate the need for mechanical alloying and to produce a more uniform distribution of NFs. The overall tasks included powder production and milling, consolidation, deformation processing, shape fabrication, joining, irradiation tolerance and property characterization and optimization. UCSB's research focused on characterizing the NFA microstructure and NFs and the corresponding effects on mechanical properties. We first

evaluated the benefits of pre-alloying Y during gas atomization in rapidly solidified Fe-14Cr-3W-0.4Ti-0.2Y (14YWT) powders and then characterized the 14YWT after each processing step of atomization, ball milling, and annealing or hot consolidation.

2.1.1 Atomized powder batches

ATI Powder Metals Laboratory (Pittsburgh, PA) produced the 14YWT atomized powders that have been further processed at ORNL and UCSB and primarily characterized at UCSB. Atomization was carried out in the ATI Laboratory Gas Atomizer (LGA) using a 27 kg nominal capacity vacuum induction melting (VIM) furnace lined with an alumina crucible that tilts to pour the melted alloy into a refractory tundish with a ceramic nozzle at the bottom. The combined effects of gravity and aspiration pressure deliver the melt through the nozzle to the gas atomization die in a close-coupled mode consisting of coaxial, co-directional supersonic gas flow to disrupt the stream of molten metal. Atomization breaks the melt stream into spheroidal droplets that solidify rapidly in a controlled atmosphere while moving through a stainless steel cooling tower.

Atomization is usually carried out in argon, but for this study an Ar/O and He atmosphere were also used. The Ar/O atmosphere was intended to increase the O content to a value of ≈ 0.16 wt.%, since O is no longer being supplied by Y_2O_3 during mechanical alloying. Helium has a greater thermal conductivity than Ar, thus was intended to increase the cooling rate. Each batch of powder was sieved to three different mesh fractions (-35/+100, -100/+325, and -325) that are designated large (L), medium (M) and small (S), respectively. The corresponding compositions are summarized in Table 2.1, which shows that the O content varied with the mesh size in all three heats and, as expected, the finest powder (-325 mesh), with the greater surface area to volume ratio,

had higher O and N content than the larger powders. The O level was approximately equal for the argon and helium atomized powders, but was ≈ 5 to 10 times higher for the Ar/O atomized batch. Since the major alloying element compositions do not vary with particle size, they were only measured for the -35/+100 mesh powder.

Table 2.1. Composition and sizes of atomized powders from ATI Powder Metals.

Heat Gas	Mesh	Wt. (kg)	Cr	W	Ti	Y	Al	Si	O	N	C
L2311 Ar	-35/+100	5.4	14.0	3.0	0.35	0.21	0.016	0.029	0.0085	0.0015	0.0020
	-100/+325	6.7	“	“	“	“	“	“	0.0140	0.0025	0.0060
	-325	4.8	“	“	“	“	“	“	0.0235	0.0080	0.0060
L2312 Ar/O	-35/+100	6.9	14.0	3.1	0.39	0.23	0.020	0.022	0.0740	0.0020	0.0020
	-100/+325	6.6	“	“	“	“	“	“	0.0960	0.0130	0.0020
	-325	6.0	“	“	“	“	“	“	0.1365	0.0095	0.0025
L2313 He	-35/+100	7.3	13.8	3.0	0.36	0.21	0.024	0.023	0.0085	0.0040	0.0040
	-100/+325	3.8	“	“	“	“	“	“	0.0110	0.0035	0.0035
	-325	2.0	“	“	“	“	“	“	0.0275	0.0130	0.0045
L237B Ar Blend	+35	-	14.0	3.0	0.36	0.21	0.025	0.020	-	-	-
	-35/+100	21	“	“	“	“	“	“	0.0090	0.002	-
	-100/+325	20	“	“	“	“	“	“	0.0136	0.002	-
	-325	16	“	“	“	“	“	“	0.0341	0.002	0.005

After the initial investigation of the Ar, Ar/O, and He powders, a second 57 kg batch of low O 14YWT powders were produced using three individual and nominally identical Ar atomization runs. The powders were first sieved to separate the very course -35 mesh powders that were then used to measure the Y, Ti, W and other substitutional solute compositions. The finer powders were blended into a master batch (L237B) that was sieved into the L, M and S mesh sizes cited above. The O content again varied with the mesh size, as expected, with the S-powder containing ≈ 0.034 wt.% O and the L-powder containing ≈ 0.009 wt.% O. Table 2.2 summarizes the analysis performed on the as-atomized powders, including compositional analysis of O and N using inert gas fusion (IGF) [3].

A selected subset of as-atomized powders were characterized by APT, EPMA and TEM. The initial TEM samples for the first batch of as-received Ar, Ar/O and He powders were prepared by mixing them with M-Bond 610 epoxy and punching resin-powder composite into 3 mm disks [4]. The disks were dimple ground and polished using a Gatan 691 ion milling system in incremental 5 to 2 keV. A standard mounting and polishing procedure was developed for all the other cases. A mortar and pestle was used to grind a phenolic, conductive polymer (Konductomet, [5]) with the 14YWT powder. The resin-coated powders were then pressed into 25.4 or 31.75 mm diameter disks, and set by heating to 250°C for five minutes at 21 MPa [5]. The discs were sanded with 220 grit paper to expose the firmly embedded powders and then vibratory polished at low speed a minimum of six hr in an ethylene glycol and 0.05 μm alumina mix [5,6]. This procedure results in mounted and polished powders that are in a form suitable for etching, FIB lift outs, microhardness measurements and EPMA.

Table 2.2. Analysis summary on as-atomized powders.

	IGF	EPMA	TEM	SANS	APT
L2311S	✓	✓	✓	✓	✓
L2312S	✓	✓	✓	✓	-
L2313S	-	✓	✓	✓	-

2.1.2 Powder milling

As discussed in section 4.1.1, TEM and EPMA showed the Y is not uniformly distributed after atomization. Thus studies were carried out to determine the milling conditions that would effectively homogenize the powders. In the first study, Ar, Ar/O, and He atomized -325 mesh powders (L2311S, L2312S, L2313S) were loaded into an O-ring sealed can with an Ar atmosphere and then SPEX shaker milled for 10h with a

hardened steel ball to charge ratio of 5:1, a ball size of 9.5 mm and a powder charge of 20 g.

A second set of powders (L2311M and L2312M) was Zoz CM01 attritor milled by UCB in ≈ 100 g batches using 5 mm hardened steel balls at a ball to powder mass ratio of 10:1. The milling speed alternated between 900 (2 minutes) and 450 rpm (9 minutes). The milling times were 1, 5, 20, and 40 hours. The initial CM01 loading procedure was to evacuate the milling chamber for five minutes followed by backfilling it with Ar. However, it was found that both the SPEX (UCSB) and Zoz (ORNL and UCB) powders picked up a significant amount of contaminant N using their respective milling procedures. In order to reduce the N contamination, the CM01 loading procedure was modified for milling the second large powder batch (L237BS). Cycles of the vacuum (10 min) and Ar backfills (5 min) were repeated three times and a positive over-pressure of Ar was maintained throughout milling period. Better milling chamber sealing procedures and higher purity Ar used in the glove box eliminated the N contamination in the case of the SPEX milling.

Subsequently, a larger 500 kg batch of L2311M powder was Zoz CM08 attritor milled at ORNL for 40 h with FeO (-10 mesh, Alpha Aesar, Part #30513) to increase the O content to ≈ 0.135 wt.%. The milling was carried out with improved parameters and procedures similar to those described above. Limited APT, TEM, SANS, EPMA, and compositional analysis were performed on selected subsets of the as-milled powders as shown in Table 2.3.

Table 2.3. Analysis summary on milled powders.

	IGF	EPMA	TEM	SANS	APT
L2311S SPEX 10 h Mill	✓	✓	✓	✓	-
L2312S SPEX 10 h Mill	-	✓	-	✓	-
L2313S SPEX 10 h Mill	-	✓	-	✓	-
L2313S SPEX 16 h Mill	✓	-	-	-	-
L2311M Attritor 1 h Mill	-	-	-	-	-
L2311M Attritor 5 h Mill	✓	-	-	-	-
L2311M Attritor 20 h Mill	✓	-	-	-	-
L2311M Attritor 40 h Mill	✓	-	-	-	✓
L2312M Attritor 20 h Mill	✓	-	-	-	-
L2312M Attritor 40 h Mill	✓	-	-	-	-
L237BS Attritor 40 h Mill low N	✓	-	-	-	✓
L2311M Attritor 40 h Mill w/FeO (PM2)	✓	-	-	-	-

2.1.3 Powder annealing and consolidation

Previous research showed that NF formation primarily depends on temperature and only weakly on time, and is similar in annealed powders and consolidated alloys that experience similar thermal histories [7]. Thus the initial studies of NF formation were carried out on annealed powders with thermal histories that mimic a HIP cycle, thus avoiding the expensive and time-consuming consolidation processing step. The milled powders were typically degassed under a vacuum of 10^{-6} to 10^{-7} Torr between 250°C and 400°C (preferred) for 4 to 12 h in quartz tubes containing a Nb getter foil. The tube was then backfilled with ½ atm of dry helium prior to melt sealing. The powders were then annealed in a Lindberg box furnace using a Eurotherm 2404 temperature controller at a specified temperature to within ±1°C. The annealing temperatures were 1100°C for the SPEX milled powders and 1150°C for the attritor milled powders with a heating and cooling rate of 15°C/min and dwell time of 3 h to simulate typical HIP consolidation

conditions. The tools used to characterize the milled and annealed powders are summarized in Table 2.4.

Table 2.4. Analysis summary on milled and annealed powders.

	IGF	EPMA	TEM	SANS	APT
L2311S SPEX Mill/1000ºC Anneal	-	✓	✓	✓	✓
L2312S SPEX Mill/1000ºC Anneal	-	✓	-	✓	-
L2313S SPEX Mill/1000ºC Anneal	-	✓	-	✓	-
L2311M 1 h Mill/1150ºC Anneal	-	-	-	✓	-
L2311M 5 h Mill/1150ºC Anneal	-	-	-	✓	-
L2311M 20 h Mill/1150ºC Anneal	✓	-	-	✓	✓
L2311M 40 h Mill/1150ºC Anneal	✓	-	✓	-	✓
L2312M 1 h Mill/1150ºC Anneal	-	-	-	-	-
L2312M 5 h Mill/1150ºC Anneal	-	-	-	✓	-
L2312M 20 h Mill/1150ºC Anneal	-	-	-	✓	-
L2312M 40 h Mill/1150ºC Anneal	-	-	✓	✓	-
L237BS 40 h Mill/1150ºC Anneal	-	-	✓	-	-
L2311M 40 h Mill w/FeO, 850ºC Anneal	-	-	-	✓	-
L2311M 40 h Mill w/FeO, 1000ºC Anneal	-	-	-	✓	-
L2311M 40 h Mill w/FeO, 1150ºC Anneal	-	-	✓	✓	-
L2311M 40 h Mill w/FeO, 1150ºC Iso-ann.	-	-	-	✓	-

Four milled powders were HIP consolidated. Two HIPed alloys, designated OW1 and OW2, were produced from ≈ 60 g each of the preliminary batch of medium-sized Ar atomized 40 h attritor milled powders (L2311M). Both were HIPed at 1150°C for 3 h at 200 MPa by American Isostatic Presses (Columbus, OH). The OW1 alloy was consolidated by HIPing the ball milled powders following standard degassing and canning treatments in 12.7 mm diameter steel 1010 low carbon, weld-sealed tubes. The OW2 alloy was consolidated using the same HIPing treatment, but in this case the as-milled powders were isothermally annealed at 1000°C for 1 h prior to HIPing. A third

consolidated alloy, OW3, was HIPed, using ≈ 200g of the second, larger batch of small, blended powders (L237BS) that were attritor milled at UCB for 40h using the modified milling procedure described above. The HIP conditions were identical to those used for OW1 and OW2, except that 32 mm 304 SS cans with solid, welded bottom plugs and top plugs with 9.5 mm tubes for evacuation and degassing were used in this case. Figure 2.1a and b shows example cans before and after HIPing. Figure 2.1c shows an example HIP can where washers separated different powders to produce consolidated material from smaller powder batches. This method was used to produce control materials for the SANS studies. The final HIPed alloy, OW4, was consolidated in the same way as OW3 using ≈ 200 g of the L2311M powder attritor milled with FeO at ORNL.

A final alloy, designated as 14YWT-PM2 (PM2), was produced from the same L2311M powder used for OW4. Consolidation and processing conditions include degassing at 400ºC, hot extrusion at 850ºC in a steel can, annealing for 1 h at 1000ºC, and then hot cross rolling to ≈ 50% thickness. The analysis performed on the four HIP consolidated alloys and PM2 is given in Table 2.5.

Table 2.5. Analysis summary on consolidated alloys.

	IGF	**μH**	**TEM**	**SANS**	**APT**
OW1	✓	✓	✓	✓	✓
OW2	✓	✓	✓	✓	✓
OW3	-	✓	✓	✓	✓
OW4	✓	✓	✓	-	✓
PM2	-	✓	✓	-	✓

a b c

Figure 2.1. 32 mm stainless steel HIP can a) before; b) after HIPing; c) example of HIPing multiple powders in a single can.

2.2 Composition and processing variations

A major goal of this research was to determine how the NFs are affected by variation in the alloy Y, Ti, and O content. The effects of O content were explored by comparing the OW1 (high O), OW3 (low O) and OW4 (intermediate O) alloys based on attritor-milled powders. The effects of Y_2O_3 content and the ratio of Ti:Y were also studied for a matrix of 12 SPEX milled powders.

Table 2.6 gives the Ti content (wt.%) of the SPEX milled alloy matrix in terms of the Y_2O_3 content (wt.%) and a Ti/Y atom ratio. The powders were prepared by SPEX milling Fe14Cr3W (wt.%) powders with varying elemental Ti and Y_2O_3. Maintaining the Y_2O_3 at 0.3 wt.% while reducing the Ti from 0.4 to 0.3 and 0.2 wt.% corresponds to Ti/Y atom

ratios of 3.1, 2.4, and 1.6, respectively. These ratios were maintained while varying the Y_2O_3 from 0.2 to 0.5 in 0.1 wt.% increments. The resulting compositions are given in Table 2.6. SPEX milling was carried out for 10 h using the Fe14Cr3W pre-alloyed powder and 15 nm Y_2O_3 powder with a 50:50 mixture (by mass) of 6 and 8 mm diameter tool steel milling balls and 10:1 ball to powder mass ratio. Annealing at 1150°C was carried out using the procedure described in Section 2.1.3.

Table 2.6. Milling matrix showing Ti wt.% for corresponding Y_2O_3 and Ti:Y ratio.

		Ti:Y (atom ratio)		
		1.6:1	**2.4:1**	**3.1:1**
Y_2O_3 (wt.%)	**0.2**	0.13	0.20	0.27
	0.3	0.20	0.30	0.40
	0.4	0.27	0.40	0.53
	0.5	0.33	0.50	0.67

Previous SPEX milled powders showed that a significant amount of O and N was introduced during mechanical alloying. The resulting O levels were sufficient to produce large NF populations, but the process was not well controlled, or amenable to systematic studies of the effects of O. For the alloys in Table 2.6, a higher purity 99.9997% Ar atmosphere was used as recommended by Ohtsuka [8]. It is likely that contamination occurred due to a compromised O-ring milling can seal. The powder with a Ti/Y ratio of 1.6 and 0.4 wt.% Y_2O_3 was milled using an improved can seal where Teflon® tape was wrapped around the can threads and a 0.8 mm thick carbon sheet was placed between the threaded ring and the top of the can. Along with the use of research grade purity Ar, this resulted in a significant reduction in O contamination.

SANS measurements were carried out on the complete powder matrix in the milled and annealed (1150ºC, 3 h) condition. Atom probe was performed on four of the twelve milled and annealed powders, and included all three Ti/Y ratios of powders with 0.3 wt.% Y_2O_3 as well as the powder milled with improved can sealing (0.4 at.% Y_2O_3, Ti/Y = 1.6).

The alloys OW1, OW3, and OW4, described above, were used to explore the effects of O on the microstructure and NFs. The alloys are referred to here and in section 4.1.2.4 as OWL (OW3), OWI (OW4), and OWH (OW1) to indicate low, intermediate, and high O contents. The first attritor milling procedure on the L2311M powder added high levels of O (and N) as contaminants (OWH). The improved attritor milling procedure at UCB greatly lowered the contamination of both N and O (OWL). However, the minimal O content in this alloy resulted in low hardness and much coarser grain and NF structures. Thus, the intermediate O alloy was produced by milling initially low O powder (L2311M) with FeO (OWI). Examining the micro-nanostructure and hardness of the three alloys provides an opportunity to assess the effects of O on a fully ferritic 14CrYWT alloy. The grain structures of these alloys were characterized by optical metallography and bright field (BF) TEM using the line intercept method to measure the average grain size and size distribution. Optical measurements were made after etching polished samples with a 3:1:1 ratio of hydrochloric, acetic, and nitric acid for 10 to 50 seconds.

2.3 Solid state joining

The emphasis of the joining study was on the atom probe tomography (APT) characterization of NFs in NFA MA957 in the as extruded (AE), FSW and FSW and

annealed at 1150°C/3 h (FSW-A) conditions. The objective is to assess the effect of severe high temperature deformation during FSW on the NFs at the near atomic scale. This issue is of natural concern, since FSW might be expected to dissolve the NFs by mechanisms that are akin to those that occur during mechanical alloying (MA). The annealing treatment was primarily intended to examine the possibility of reprecipitating some of the Y–Ti and O that might dissolve during FSW.

Plates with dimensions of 100 mm × 17 mm × 2 mm were sectioned and butt FSW in the long dimension direction at a tool spindle speed of 130–160 rev min^{-1} and travel speed of 150–200 mm min^{-1}. Coupons were removed from the middle of the FSW zone. One coupon was annealed at 1150°C for 3 h while wrapped in Fe–Cr metal foils inside a sealed quartz tube to minimize Cr loss, oxidation and impurity pick-up. The as extruded, FSW and FSW-A conditions were characterised by APT, TEM and Vickers microhardness measurements.

2.4 Target of opportunity irradiations

A task in this program was participation in various target of opportunity irradiation experiments. The primary focus of these studies includes US and French heats of MA957 (Fr-MA957). US MA957 25 mm diameter as-extruded round bar was acquired from Pacific Northwest National Laboratory (PNNL). While INCO's mechanical alloying and consolidation parameters for US MA957 are proprietary and are not known in specific detail, the original patent gives likely processing parameters. Phase blended -40 and -80 mesh (≤ 400 μm and ≤ 177 μm) Fe-based compound powders for each alloying element were mechanically alloyed with Y_2O_3 powders by attritor milling for 24 h at 288 rpm using a 20:1 ball to powder mass ratio. Canned powders were hot extruded at 1065ºC

with a 6:1 ratio. The Fr-MA957 heat is in the form of a 9 mm thick, 65 mm outer diameter tube for CEA/Saclay in France by center drilling a MA957 bar followed by hot extrusion. This heat was acquired via Oak Ridge National Laboratory. The nominal composition of MA957 is shown in Table 2.7.

Table 2.7: MA957 nominal composition in wt. %.

Fe	**Cr**	**Ti**	**Mo**	**Y_2O_3**
Bal.	14.0	1.0	0.3	0.25

The remaining focus for including NFA alloys in irradiations was on alloy U14YWT along with a small group of 9-15 Cr NFA alloys supplied by other institutions. U14YWT is a Fe14Cr3W0.4Ti0.3Y_2O_3 alloy produced at UCSB using a SPEX shaker mill. The alloy was HIP consolidated at 850ºC, 1000ºC and 1150ºC with final designation U14YWT-A, B and C, respectively.

A large specimen set was prepared for the irradiation experiments. Disk multi-purpose coupons were the most common specimen type and are typically 0.2 or 0.5 mm thick for use in microhardness measurements, shear punch testing and general microscopy. A variety of compact tension, bend bar and tensile specimens were also included for a subset of the material and irradiation conditions. Finally, many small disk in situ He implanter specimens were prepared to assess He effects and management. Table 2.8 gives the range of dpa and temperature for the irradiations in the Advanced Test Reactor (ATR), the JOYO sodium cooled fast reactor, the High Flux Isotope Reactor (HFIR), and the SINQ spallation neutron source for the SINQ Target Irradiation Program (STIP). An approximate specimen count is also shown.

Table 2.8. Target of opportunity irradiations.

Irradiation Experiment	dpa Range	Temperature Range (ºC)	Total Specimen Count
JOYO	1.5 - 7	453 - 668	56
STIP VI	3 - 22	400 - 650	115
ATR	1.7 - 6.2	290 - 750	492
HFIR	10 - 60	300 - 650	609

3.0 Summary of the Characterization Techniques

Due to the small size of the Y-Ti-O NFs in NFAs, characterization is difficult and requires a suite of tools. Even using a toolkit of state of the art techniques, the identity of the smallest NFs is still a matter of doubt and controversy. The techniques employed in this research include small angle neutron scattering (SANS), transmission electron microscopy (TEM) and atom probe tomography (APT). A host of other methods, including electron probe micro-analysis (EPMA), were used to assess larger length scale microstructural and compositional characteristics of the NFA. A limited amount of mechanical property data was acquired using microhardness, while tensile, creep and fracture toughness measurements have commenced and are continuing under a new NEUP program.

3.1 Small angle neutron scattering

The SANS measurements were performed at the NIST Center for Neutron Research in Bethesda, MD on the NG7 SANS instrument [9] at a neutron wavelength of $\lambda = 0.5$ nm with the two-dimensional ^{3}He detector located 1.54 m from the sample and offset by 20 cm to increase the q-range up to more than 3 nm^{-1}. The differential scattering cross section $d\Sigma(q)/d\Omega$ of the scattering features were derived from two-dimensional scattering measurements on coupons or powder packets in a 1.7 T horizontal magnetic field. The magnetic field permits measurement of both nuclear (n) and magnetic (m) scattering, where the latter depends on the angle from the horizontal magnetic field direction, q, as.

$$d\Sigma(q)/d\Omega(q)_{tot} = d\Sigma(q)/d\Omega_n + \cos^2(q)d\Sigma(q)/d\Omega_m \quad (1)$$

Approximately 5 million detector counts were acquired for each run. The measured intensity was converted to an absolute differential scattering cross section, $d\Sigma(q)/d\Omega$, by subtracting background and empty container scattering and using the sample mass and measured transmission to normalize and calibrate the scattering intensity data to a water standard. The NF scattering was determined by subtracting the $d\Sigma(q)/d\Omega$ for a control that did not contain Y. Eq. 1, was used to derive $d\Sigma(q)/d\Omega_n$ and $d\Sigma(q)/d\Omega_m$ from the $d\Sigma(q)/d\Omega$ data averaged over the entire detector range of q and θ to evaluate magnetic to nuclear scattering ratio, $d\Sigma(q)/d\Omega_m/d\Sigma(q)/d\Omega_n = M/N(q)$. The M/N were also evaluated by fitting $d\Sigma(q)/d\Omega$ averaged over a wide q-range as a function of $\cos^2(\theta)$. Log plots of the averaged $d\Sigma(q)/d\Omega$ data as a function of q^2 for three θ, where θ = 0 ± 30°, 45 ± 15° and 80 ± 10°, were also used to present and examine the data.

The $d\Sigma(q)/d\Omega$ for features with a size r, volume V and number density N, is given by

$$d\Sigma(q)/d\Omega) = NV^2(\Delta\rho)^2\{3[\sin(qr) - qr\cos(qr)]/(qr)^3\}^2 \qquad (2)$$

The $\{\}^2$ term is the form factor for well-separated spheres. Here Δρ is the scattering length density difference between the matrix and NF, Δρ = ρ (mat) - ρ (nf). The ρ values are the known magnetic or nuclear scattering length for a specified isotope divided by the atomic volume. Since the composition and atom volume in the NFs, hence the nuclear scattering contrast, $\Delta\rho_n$, are unknown, $d\Sigma(q)/d\Omega_n$ cannot be used to analyze the SANS data. However, the Y-Ti-O NFs are unlikely to be magnetic, and this assumption has been verified by measuring the temperature dependence $d\Sigma(q)/d\Omega_m$ [7,10]. Assuming the NFs act as magnetic holes in a saturated Fe-Cr ferromagnetic matrix allows the $\Delta\rho_m$ =

$\rho(mat)_m$ which is known; note, this requires properly accounting for the alloy composition on the matrix magnetization [7,10]. The distribution (Δr) and average size ($<r>$) of the NFs, their number density (N), and their corresponding total volume fraction, (f), were derived by least squares fitting computed scattering curves (Eq. 2) to the measured $d\Sigma(q)/d\Omega_m$ data, assuming a log-normal size distribution. In some cases the M/N varied significantly with q and assuming a single scattering feature over the entire q range did not provide a good fit to the data. In these cases the $d\Sigma(q)/d\Omega_m$ data was fit to two features with different $<r>$, Δr and M/N. Typically the second feature was very small with $<r> \leq 0.5$ nm and a low $M/N < 1$. It is not clear if these small features are real, or if they are artifacts of the approximate control subtraction procedure. In any case, the first larger features are assumed to represent scattering from the actual NFs. Further details on the data analysis is described elsewhere [7-11].

The M/N ratio also contains information on the NF composition due to its effect on the nuclear but not magnetic scattering. The composition cannot be uniquely determined from the M/N ratio, but the measured M/N can be compared to calculated M/N from NFs with assumed compositions and densities such as the equilibrium bulk oxide phases $Y_2Ti_2O_7$ and Y_2TiO_5. The measured M/N, however, is to some extent affected by the approximation associated with subtracting a control that may not fully represent the scattering not associated with the NFs. Further, the assumption that the matrix is magnetically saturated may not be fully valid in some cases.

3.2 Atom probe tomography

APT was performed using an Imago Local-Electrode Atom Probe (LEAP) 3000X HR. Samples are prepared either by electropolishing or as lift-outs using an FEI Helios 600 focused ion beam (FIB). Electropolished samples were made from ~0.5 mm x 0.5 mm x 20 mm bars using the two stage process described by Miller [12]. FIB sample preparation used the trench method outlined by Thompson [13]. Each sharpened tip is cleaned to remove Ga damage first using a 5KeV and then a final 2 KeV beam at 28 pA. The LEAP samples were examined in voltage or laser mode for a variety of run conditions. Temperatures ranged from 33K to 60K and laser pulse energies varied from 0.05 nJ to 0.45 nJ with a green (λ = 532 nm) laser. Laser and voltage pulses were held at 200 kHz repetition rate, the evaporation rate was typically between 0.5% and 1%, and in voltage mode the pulse fraction was either 20 or 25%.

The Imago Interactive Visualization and Analysis Software (IVAS) package was used for reconstruction and analysis of the LEAP data. To improve accuracy of the reconstruction, SEM images of the needle profile (52° stage tilt) were taken at the start and, when possible, at the end of the run. The actual length of the field evaporated region was determined by superimposing ovals representing the pre- and post-run tip radii onto the SEM image and comparing the measured length with the length of the IVAS reconstructed data. If the lengths did not match, the default evaporation field (Fe = 33 V/nm) was adjusted until the IVAS reconstruction length agreed with the measured value from the SEM. The newest version of the IVAS software has a built in tool for performing this operation.

Analysis of APT data requires identifying all pertinent ion mass to charge ratios (m/c) that form a wide spectral distribution composed of specific isotopes and charge states, including ionic species, like TiO^{+2}, are also frequently field evaporated. The identity of an atom or ionic species is determined from the background-subtracted spectrum with m/c increments assigned to a particular peak in a process called ranging. The m/c spectrum is influenced by a large number of variables, such as voltage versus laser mode, specimen temperature, laser energy and even variations in the specimens themselves. Identifying the m/c peaks can be challenging because complex iron alloys have many overlapping and interfering peaks in their m/c spectrum. However, elements like Fe, Cr, and Ti have a number of isotopes, resulting in multiple peaks with some that are more isolated. The multiple peaks were exploited to better estimate the total number of ions based on the natural isotope abundance ratios using a method called de-convolution. This method allows a more accurate ion count, but ion position in the reconstruction cannot be determined separately for each ion species in a single peak. Large post-peak tails from Fe^{+2} isotopes with mass numbers from 54 to 60 are also a problem because they overlap the peaks for Y^{+3} and to a lesser extent TiO^{+2}. The number of ions in these smaller peaks was characterized using the side-band method of systematic background subtraction of the major element tails [14]. After background subtraction the peaks are generally isolated although their corresponding ion count still has an associated uncertainty.

The NFs were identified using both isoconcentration surfaces and the maximum separation distance methods [15,16]. The total number of precipitates was counted by adding the number of complete precipitates to one-half of the precipitates on the edge of the data set [12], and was used to determine the number density as

$$N_d = \frac{N_p \zeta}{\Omega N} \quad (3)$$

Here N_p, ζ, Ω, and N are the number of precipitates, the detector efficiency (37%), the atomic volume (based on bcc iron with a lattice parameter of 0.288 nm), and the total number of ranged ions, respectively. The size and composition of the NFs was determined using the maximum separation method for the solute ions of interest, namely Y, Ti and O, including their ionic forms like TiO^{xx} and YO^{xx}. The radius of gyration (l_g) is one method for determining the size of precipitates and is equal to the distance from the precipitate center to a radial distance containing the entire mass of the precipitate as shown in Eq. 4 [12]. Here, n_i is the number of atoms at, r_i, which is the atom's distance from the center of mass, and n is the total number of atoms in the cluster. This so-called radius of gyration is related to the actual physical radius of the cluster r, as $r = 1.29 l_g$ [12,17].

$$l_g = \Sigma n_i r_i / n \quad (4)$$

Consistent with other studies [18,19], the clusters were found to nominally contain significant quantities of Fe and Cr. This is believed to be an APT artifact associated with trajectory aberrations caused by different evaporation fields between the matrix and the clusters [18,19]. If, as is the case for the NFs, the species in the cluster have lower evaporation fields, they are emitted preferentially and earlier than the matrix ions. This causes a dimple shaped local topology change in the needle tip, that images as a dark region in field ion microscopy micrographs. In this case, the cluster species and adjoining matrix ion trajectories overlap (are mixed with) one-another. An increase atom density in

the cluster signals this condition. In contrast to the actual sequence of ion emissions, the reconstruction algorithm assumes the atoms are uniformly emitted from the tip of the needle one layer at a time in the z-direction. The consequences of this approximation are further discussed below with a specific example.

However, as a practical matter, the excess Fe should be removed in establishing the cluster compositions. If other information suggests that the cluster is unlikely to contain any significant quantity of Fe, then a practical expedient is to simply remove it in estimating the cluster composition, using only the solute content. High concentrations of matrix solutes, like Cr, are also artificially enriched in the clusters. Examples of other APT artifacts, include the possibility of pre-emission of some species that are then not detected, surface diffusion, perhaps stimulated by the high electric fields and the presence of low index pole dead zones, fine scale structures like precipitate-matrix interfaces, surface ledges and ledge kinks, uneven temperature distributions during the laser pulse and several others. Indeed, given the local variations in the binding energies of various atoms in a cluster, the overall emission process inherently involves a wide range of evaporation potentials. In the present case, a variety of these aberrations appear to be operative. The Y is concentrated in the center of the clusters while the Ti and especially the O atoms are nominally more diffuse. A corrected composition can be found by completely removing the Fe and other matrix elements (e.g., Cr) based on the ratios of the solute to Fe in the matrix [18-20]. It is not necessary to carry out deconvolution on the m/c spectrum of clusters removed from the matrix, since the overlapping peaks and post peak tails overlapping the peaks of the major elements in the cluster m/c spectrum are greatly reduced.

3.3 Transmission electron microscopy

The nanoscale features were observed in both thin TEM foils and on extraction replicas. Precipitates were extracted from the NFAs by etching the surface, applying a 10-20 nm carbon coating, and then electrochemically removing a deposited carbon film with a solution of 1% tetra methyl ammonium chloride-10% acetyl acetone-methanol. Thin TEM foils were prepared in an FEI-Helios-FIB using the lift-out technique or by twin jet electropolishing. The final thickness of the thinned foils was between 30 and 70 nm. A final, low energy Ga beam (2kVand 5.5pA) cleaning step was used to remove the high-energy ion damage to achieve high quality samples. Scanning transmission electron microscopy (STEM) high angle annular dark field imaging (HAADF) studies were performed using an FEI TITAN at 300 kV. Conventional bright field scattering contrast (diffraction contrast) TEM imaging and high-resolution transmission electron microscopy (HRTEM) imaging (phase contrast) studies were performed on either an FEI TITAN at 300 kV or an FEI T20 TEM/EDX at 200 kV. EDX spectra were recorded in STEM mode with the stage tilted to alpha=10˚, at a spot size of 3 or 4, and condenser aperture of 70 μm, which is the optimal experimental condition for taking EDX data from such small features. The analysis of the HRTEM images was carried out by fast Fourier transformation (FFT). The lattice spacing and inter-planar angles were measured by using Image J and Adobe Photoshop 6.0.

3.4 Other techniques

Luvak Inc. (Boylston, MA) provided O, N, and C composition analysis of the powders following ball milling using inert gas fusion (IGF). In addition to TEM and APT sample preparation, the FEI Helios 600 FIB was used to observe the grain structure in the

annealed powders. By imaging a broad surface area of the sample, contrast between the grains is created due to non-uniform milling of the different crystal orientations. The distribution of key solutes, such as Y, were measured on a Cameca SX-50 electron probe micro-analyzer (EPMA) fitted with 5 wavelength spectrometers and a PGT X-ray energy dispersive detector. The powders were mounted in a conductive polymer and polished to a 0.05 μm finish. Three to five measurements were made on each powder particle. Overall a total of 15 to 45 data points for each of the as-atomized, ball milled and annealed conditions for the three atomization atmospheres. Forty to fifty indents at loads from 300 to 500 g were made for the microhardness measurements, using a Vickers indenter on a LECO M-400A semi-automated hardness tester.

4.0 Summary of Results: Developing A Larger Best Practice Heat of 14YWT, NFA Optimization and NF Characterization

4.1 Developing A Larger Best Practice Heat of 14YWT

As noted previously, one objective of this study was to develop new and improved processing paths for the production of larger, best practice heats of NFAs. The work occurred in three stages: evaluating the feasibility of Y solute trapping during atomization; determining how the new processing paths affect the formation of NFs in annealed powders; and characterizing the NFs and material properties of consolidated alloys.

As discussed in section 2.1, the powders are designated L2311, L2312, L2313, and L2317B corresponding to atomization atmospheres of Ar, Ar/O, He, and the second, blended batch of Ar atomized powder, repsectively. Since including the Y during atomization did not produce a uniform Y distribution, SPEX ball milling was performed at UCSB for 10 h and Zoz attritor milling was performed at UCB and ORNL for times between 1 and 40 h. The NFs were observed in annealed powders and consolidated alloys that used both HIP consolidation (American Isostatic Presses, Columbus, OH) and hot extrusions (ORNL).

4.1.1 Composition and solute distribution and microstructure

4.1.1.1 EPMA and Chemical Analysis

EPMA studies on the L2311S, L2312S, and L2313S as-atomized and ball milled powders were performed with special emphasis on characterizing the Y distribution. As illustrated in Figure 4.1, Ar atomization does not produce a uniform Y distribution. The average concentrations of Y and corresponding standard deviations are 0.214±0.170,

0.215±0.474, and 0.154±0.089 wt.% for the Ar, Ar/O, and He as-atomized powders, respectively. The He atomized powder showed the smallest Y variability, but it was still significant. As illustrated in Figure 4.1b, the Y distribution in the Ar powder is much more homogeneous after SPEX milling. The average concentrations of Y and corresponding standard deviations of 0.206±0.027, 0.250±0.048, and 0.196±0.035 wt.% for the Ar, Ar/O and He 10 h milled conditions, respectively.

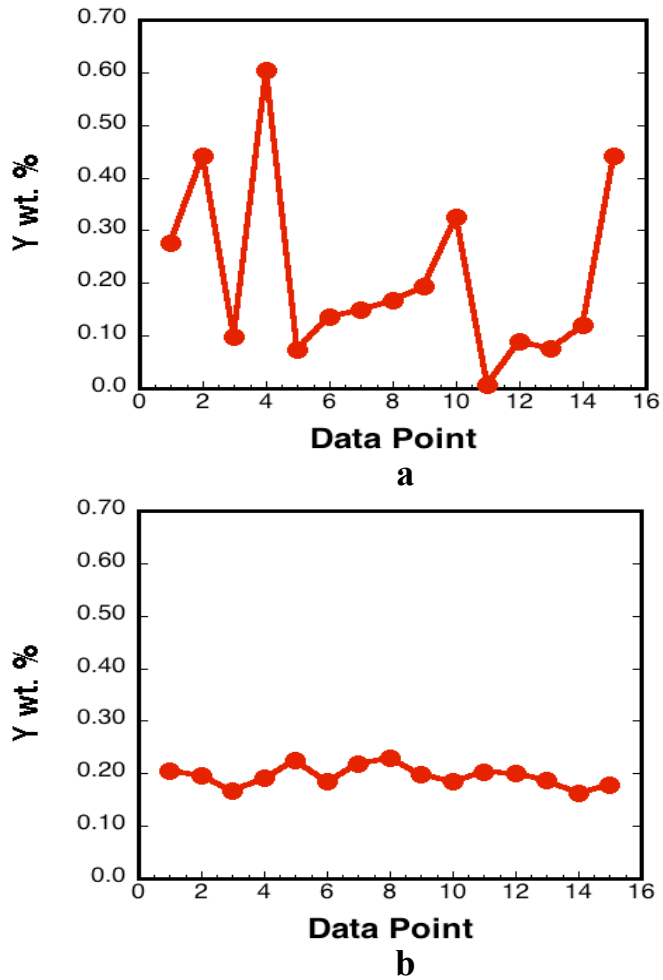

Figure 4.1. EPMA analysis of the Y concentration in a) Ar as-atomized powder L2311S; b) after 10 h SPEX milling.

The W was uniformly distributed with average compositions of 2.62±0.059 and 2.54±0.049 wt% for the He atomized powders before and after milling, respectively. The corresponding Ti concentration in the He as-atomized powder was 0.365±0.043 and the

distribution was improved after SPEX milling to 0.367±0.013 wt%. ORNL found even greater variation in the Ti content for the as-atomized condition in the L2311M (larger) powders.

Bulk chemical analysis of the L2311 Ar atomized -100/+325 mesh powders showed a minor increase in C content after milling, but a significant increase in O and N. For example, Figure 4.2 shows the systematic increase of N from 0.002 wt.% in the as-atomized powders to 0.190 wt.% after attritor milling for 40 h. The O increases rapidly during milling, reaching a 0.25 wt.% plateau after only 5 h. Similar results were observed after milling the Ar/O atomized powder for 20 and 40 h. The O contamination was 0.328 wt.% in the 20 h mill and 0.280 wt.% in the 40 h mill. The higher O contamination from the shorter milling time may indicate that contamination depends on how the milling chamber is loaded and Ar backfilled in an individual milling run. In contrast to O, the N contamination increased with the milling times at 20 to 40 h going from 0.071 wt.% to 0.200 wt.%.

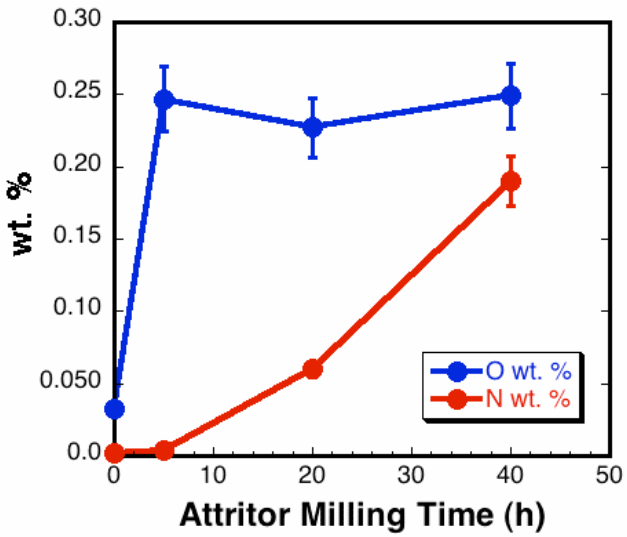

Figure 4.2. Variation on the O and N content in Ar atomized L2311M powders as a function of milling time.

Similar N and O impurity pickup occurred during SPEX milling. The O and N content after 10 h SPEX milling of the Ar atomized powder was 0.161 and 0.210 wt.%, respectively. Some of the He atomized powder was SPEX milled for a total of 16 h in 2 h increments to remove powder conglomerated on the chamber walls. The O and N content were 0.272 and 0.160 wt.% in this case, respectively. Here the O content was higher than the 10 h SPEX milled powder, but the N contamination was lower.

The N and O impurity pickup in the SPEX mill was apparently partially due to the fact that the single O-ring seal was not sufficient to prevent air leakage into the milling chamber during milling. As described in section 2.2, an improved can seal and higher purity Ar cover gas can reduce the contamination during milling. As explained in section 2.1.2, a modified attritor milling procedure successfully decreased the N and O contamination by increasing the number of vacuum and backfill cycles before commencing the milling operation. The compositional analysis in Table 4.1 shows the measured N, O, and C using the original and modified milling procedure.

Table 4.1. Interstitial composition in Ar atomized powder after milling for 40 h comparing two milling procedures.

wt.%	Original Procedure	Modified Procedure
Nitrogen	0.190	0.016
Oxygen	0.249	0.065
Carbon	0.027	0.023

Both SPEX and attritor milling caused a modest increase in the C content from 0.002 in the as-atomized condition (L2311S) to between 0.018 and 0.028 wt.% after milling. The SPEX milling for 10 h resulted in slightly less C contamination than attritor milling for 40 h. Both powder annealing and consolidation had little effect on the O and N contents. The O and N content for some of the consolidated alloys are given in Table 4.2.

The annealed OW3 powder equivalent had reduced O and N content due to the improved attritor milling procedure and that the O level was successfully increased in OW4 by milling with FeO.

Table 4.2. O and N content (wt.%) for OW1, OW2, OW3, and OW4

Alloy	**O (wt.%)**	**N (wt.%)**
OW1	0.249	0.210
OW2	0.251	0.190
OW3 (powder)	0.065	0.016
OW4	0.127	0.013

4.1.1.2 TEM and APT characterization

Consistent with the large Y variation observed in the EPMA data, TEM and EDX verified the presence of 5 nm to 100 nm phase separated Y in all of the Ar, Ar/O and He as-atomized powders. Both spherical and elongated precipitate morphologies were observed, and there were indications of both intermetallic (e.g., Y_2Fe_{17}) and complex yttrium oxide phases in the Ar/O as-atomized powders (L2312S) and regions containing very fine ≈ 5 nm precipitates were observed in the Ar as-atomized powder (L2311S). However, These precipitates were too small for EDX analysis.

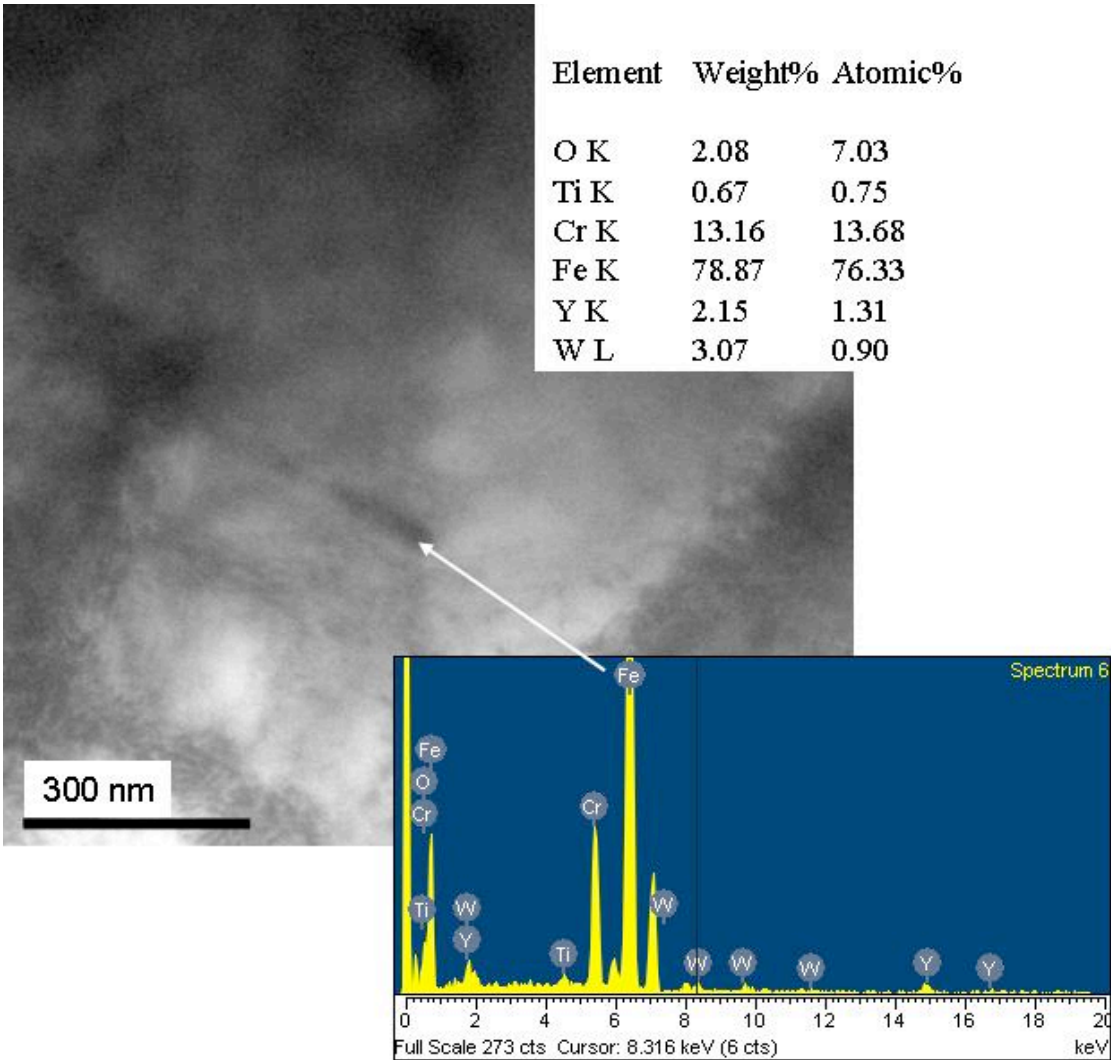

Figure 4.3. Bright field image and EDX spectrum of an elongated Y-rich precipitate in He atomized L2313S powder.

An example of an elongated Y-rich precipitate in the He as-atomized -325 mesh (L2313S) powder is shown in Figure 4.3. The EDX spectrum shows elevated concentration of both Y and Ti in this case. The true composition of the precipitate is difficult to determine since the majority of the EDX signal is from the matrix. Another example of Y-rich phases in the Ar atomized powder is shown in Figure 4.4. ORNL also observed Y rich intermetallic phases on the grain boundaries.

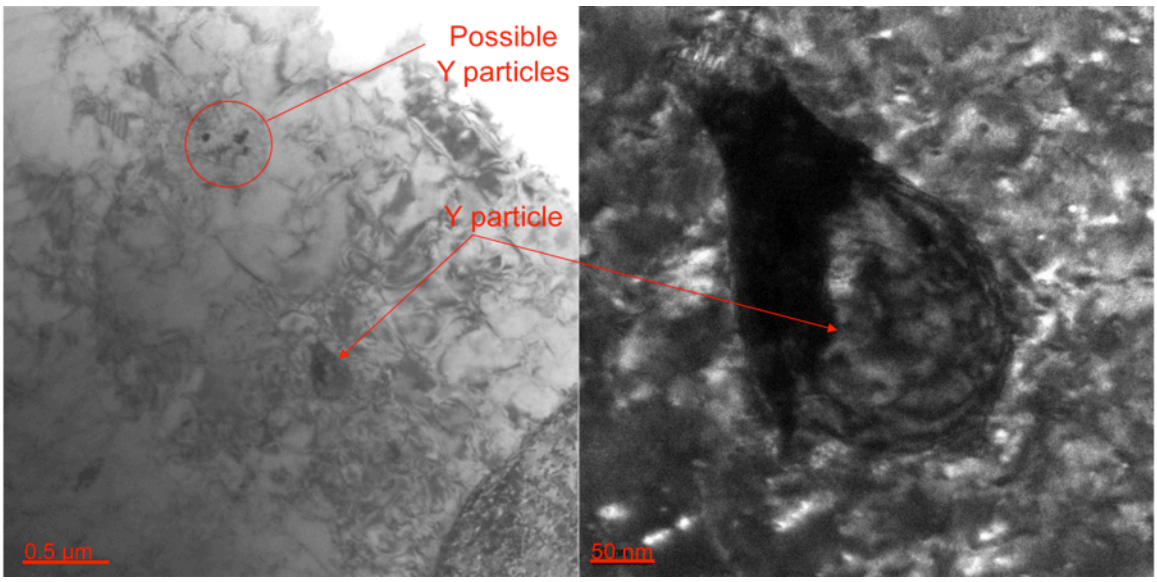

Figure 4.4. Y precipitates in Ar atomized (L2311S) powder.

APT was performed on the Ar as-atomized powder. The 10 nm thick atom maps in Figure 4.5a show that Fe, Cr, W and Ti are reasonably uniformly distributed in the matrix. The m/c spectra in Figure 4.5b contain Ti, Cr, and Fe peaks, but no Y peak was observed. The overall composition for this sample given in Table 4.3 agrees well with the chemical composition of the powder except for the absence of Y and lower Ti in the APT measurement. The absence of Y is expected since the large size and low number density of Y rich precipitates and Y_2Fe_{17} intermetallic phases make it unlikely for them to be found in the small volume analyzed.

Table 4.3. Composition comparison between APT and chemical analysis supplied by ATI Powder Metals of as-atomized powder (L2311S).

at.%	Fe	Cr	W	Ti	Y	O	C	N	Al	Si
Chem.	82.91	15.15	0.918	0.411	0.133	0.229	0.094	0.064	0.033	0.058
APT	83.40	15.18	0.898	0.243	-	0.118	0.004	-	0.025	0.057

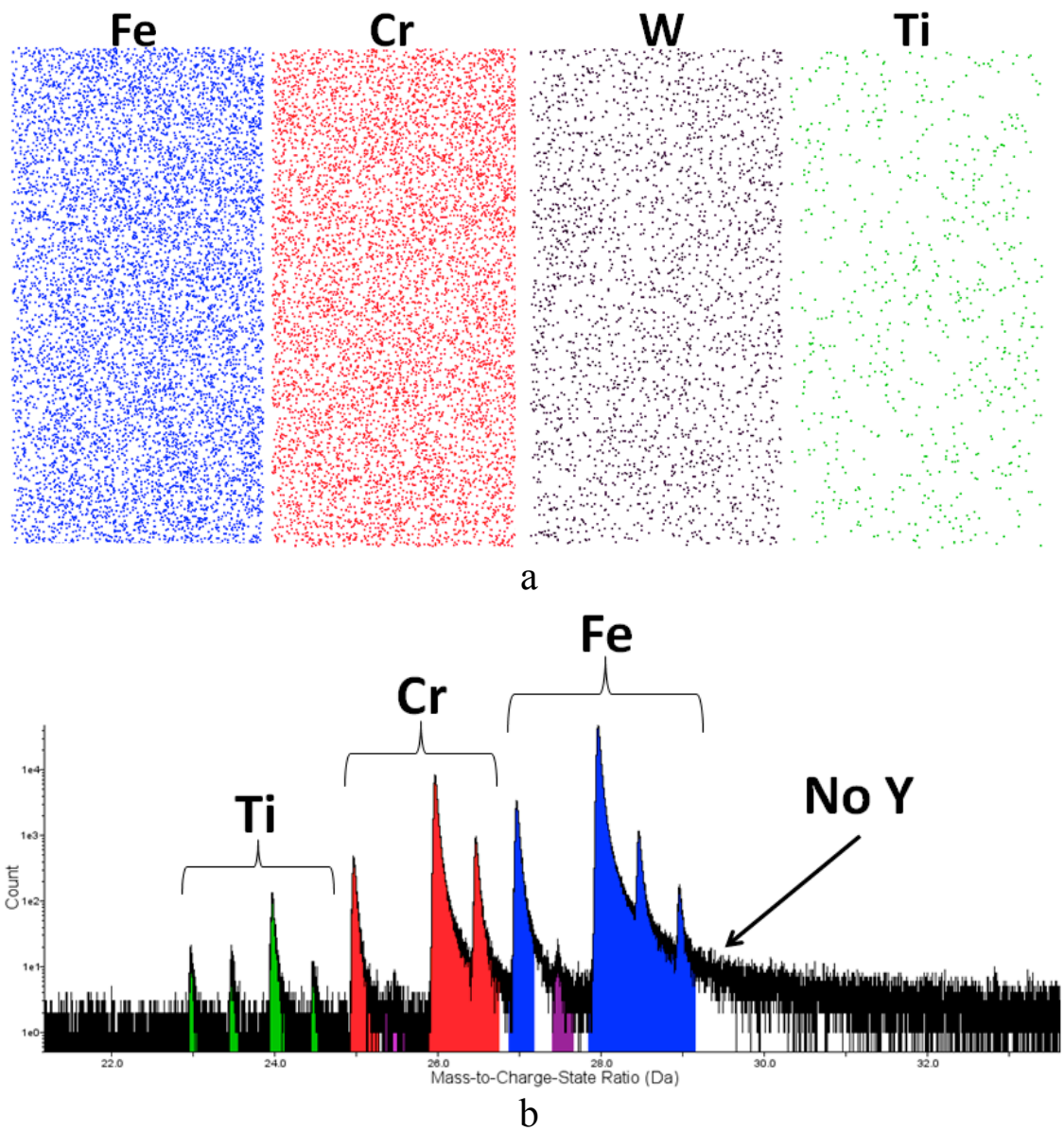

Figure 4.5. a) 10 nm thick by 20 nm X 40 nm atom maps showing uniform distribution of Fe, Cr, W, and Ti; b) mass spectrum showing no Y.

APT was performed on the 40 h attritor milled powder to determine the Y, Ti, O, and other solute distributions and associations after milling but prior to annealing. As shown in the 10 nm thick atom maps in Figure 4.6a, no distinct precipitates were found but the solute atoms appear to segregate to grain or dislocation cell boundaries spaced ≈ 10-50 nm apart that are created by severe deformation. Notably, the Y is not highly associated with the Ti or O, except where the O is included with Y and Ti as a complex ion.

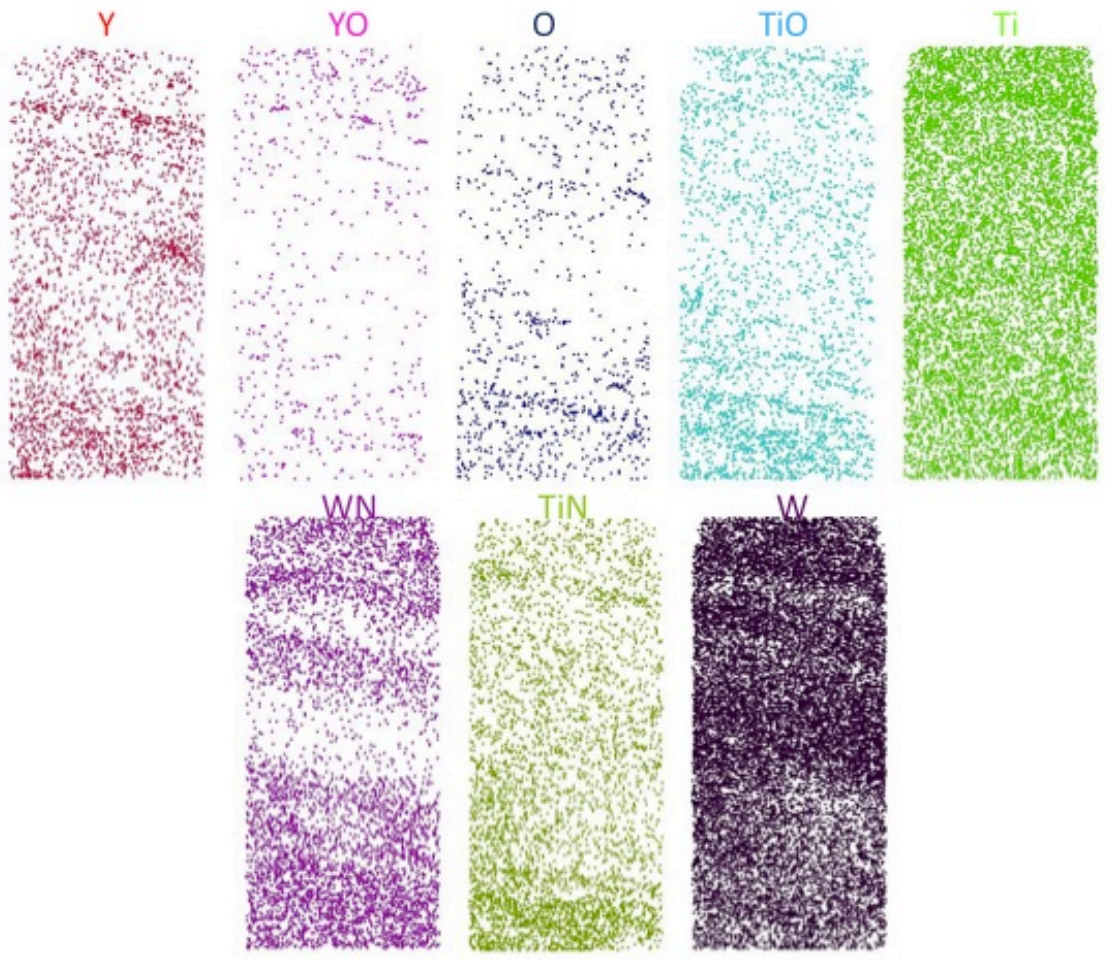

Figure 4.6. Atom maps of 40 h as-milled Ar atomized L2311M powder showing solute dissolution with some enrichment on boundaries, and associations of YO, TiO, and WN and TiN ions. The reconstruction volume is 10 nm x 20 nm x 40 nm.

As shown in Figure 4.7, TiN and WN ions were identified in the m/c as extra peaks near the TiO^{+2} and W^{+2} peaks. TiN and WN ions, present because of N contamination, are shown in the atom maps in Figure 4.6. The local N concentration in the volume sampled by APT was 0.45 at.% compared to 0.76 at.% measured by inert gas fusion (0.19 wt.%).

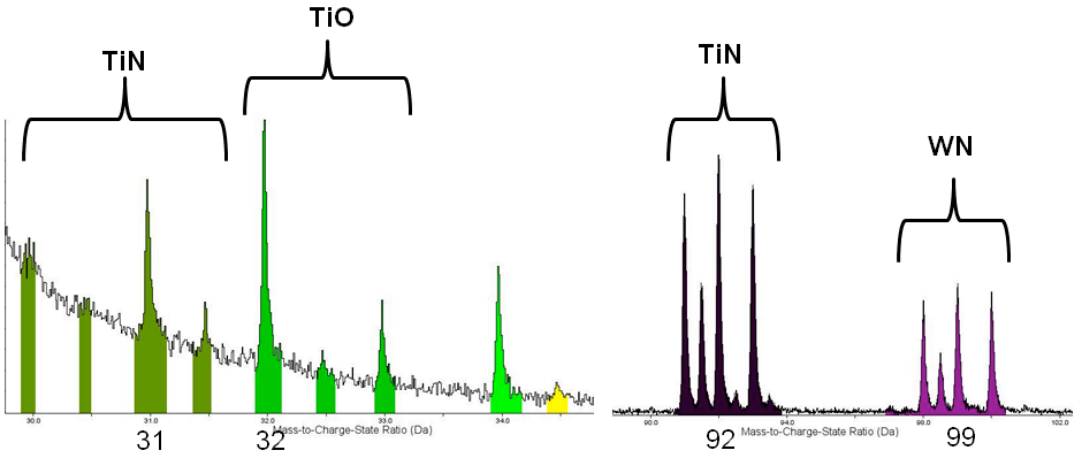

Figure 4.7. Mass spectrum of L2311M powder attritor milled for 40 h showing TiN and WN peaks.

The N contamination resulted in the formation of large Ti-N rich precipitates in the annealed powders and consolidated alloys. Figure 4.8 shows an iso-density surface of part of a large Ti-N rich precipitate in the Ar-atomized L2311S SPEX milled and annealed powder. The Ti-N precipitate appears to have a cubic polyhedral shape. A smaller, Al-O rich precipitate is associated with the larger titanium nitride. A few smaller (< 10 nm) Ti-N precipitates were also observed in the APT measurements.

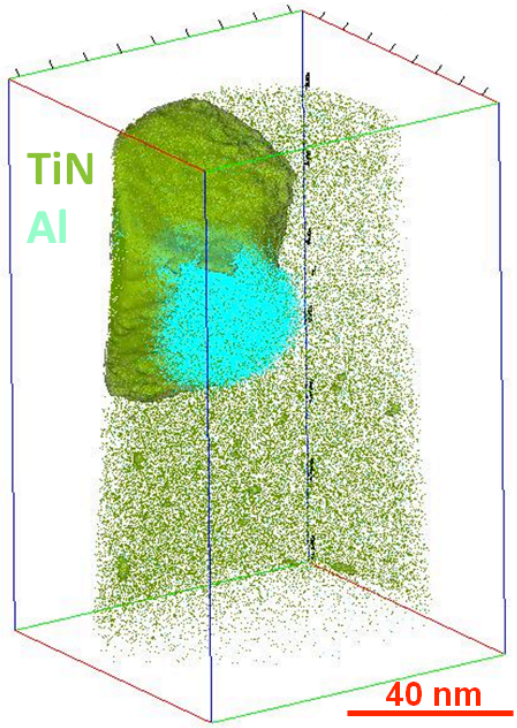

Figure 4.8. A nitrogen iso-density surface (1.35 solute atom/nm^3) for a large nitride precipitate along with TiN and Al ions showing an associated aluminum oxide precipitate.

Table 4.4 shows the nominal compositions of the associated precipitates in Figure 4.8, along with the composition of another large Ti-N precipitate found in OW1. The Ti-N rich precipitate in Figure 4.8 also contains a significant amount of Si, Cr and Fe, along with smaller quantities of O and Al, and has a Ti/N ratio ≈ 1.9. The Ti-N feature in OW1 has less Fe and Si and a higher Ti and Ti/N ≈ 3.6. After annealing and consolidation in the OW1 and OW2 alloys, the elemental Ti^{+2} ion fraction was greatly reduced compared to the as-atomized Ar powders. This indicates that almost all of the Ti is associated with either the Y-Ti-O NFs or the larger Ti-N and Ti-O (see below) precipitates. The Al-O precipitate nominally contains a large quantity of Fe. The Cr is slightly depleted compared to the matrix while Ti, Y and to a smaller extent Si are enriched. The nominal fraction of Al + O is ≈ 0.5 and the Al/O ≈ 0.76.

Table 4.4. Composition of two large Ti-N and one associated Al-O rich precipitates.

at.%	Fe	Cr	W	Ti	Y	O	C	N	Al	Si
Ti-N 1	16.5	14.7	0.40	34.1	0.37	3.8	0.060	18.0	2.33	9.22
Ti-N 2	7.3	15.5	-	54.6	0.03	3.6	0.08	15.3	-	3.6
Al-O	33.0	12.6	0.82	8.9	0.56	23.3	0.08	0.30	17.7	1.73

As shown in Figure 4.9, large 20 and 100 nm Ti-Si-O rich precipitates are also observed in the OW1 and OW2 alloys. EDX analyses of the precipitate compositions are shown in Table 4.5. There are large variations in the nominal contents of all the elements, but ignoring the matrix (Fe and Cr) and minor constituents, the average composition of these features is 56 O, 19 Ti and 25 Si in at.%. There are also variable and smaller enrichments in Al and Y.

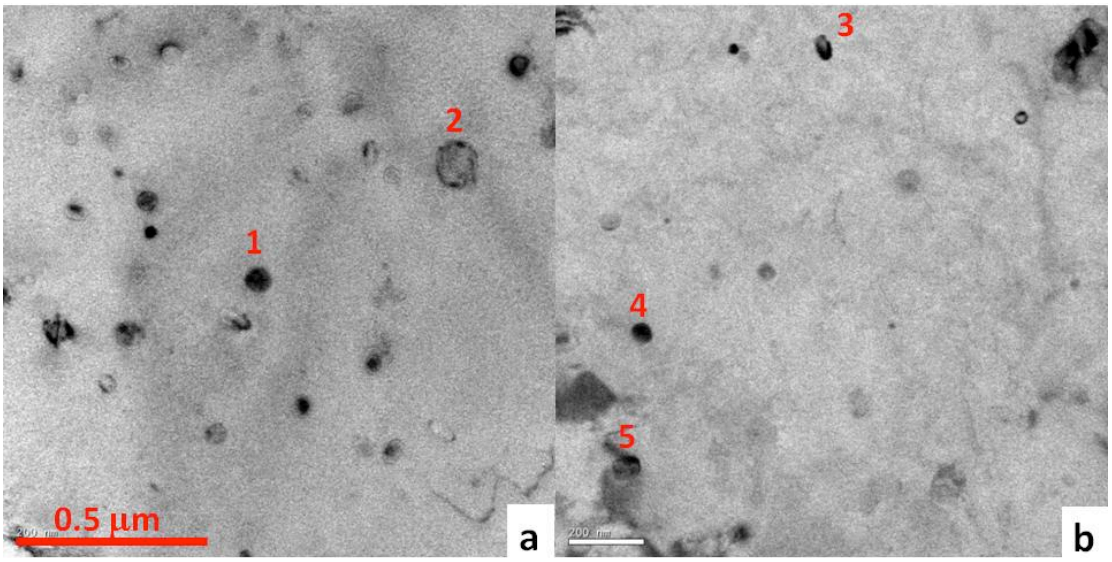

Figure 4.9. BF TEM images showing large Ti-O precipitates in a) OW1 and b) OW2.

Table 4.5. Composition of five large Ti-Si-O rich precipitates in OW1 and OW2.

at.%	Fe	Cr	O	Ti	Si	W	Y	Al
1	49.4	15.2	11.3	13.9	8.09	1.37	0.47	0.35
2	22.9	14.6	47.6	5.33	7.92	0.22	-	1.83
3	38.6	10.8	21.7	11.9	15.5	0.49	0.67	0.36
4	49.3	11.2	23.8	4.94	10.6	0.44	-	-
5	38.3	9.54	26.8	8.13	16.0	0.78	0.61	-

The APT mass spectrum in Figure 4.10 shows that the 40 h L237BS powder using the improved milling procedure did not contain WN and TiN peaks, consistent with the bulk chemistry measurements shown in Table 4.1. The O was 0.16 at.% in this case, which is lower than the 0.26 at.% observed in the 40 h attritor milled L2311M contaminated powder. The reduction in O is consistent with the bulk chemical composition, but is lower than the 0.22 at.% O (0.065 wt.%) measured by inert gas fusion (IGF). This difference is likely due to the fact that atom probe only observes a small volume that is not necessarily representative of the bulk. Figure 4.11 shows atom maps from the L237BS powder. Some Y is segregated at a boundary but otherwise is reasonably well distributed. Consistent with the solute distribution in the milled powder in Figure 4.6, the Y is not highly associated with the O and Ti.

Chemical composition [at%]

Fe	Cr	Si	V	C	P	O	Al	Ti	Co	Y	Ni	Mn	W
81.21	16.62	0.07	0.01	0.06	0.02	0.16	0.16	0.50	0.02	0.10	0.04	0.03	1.00

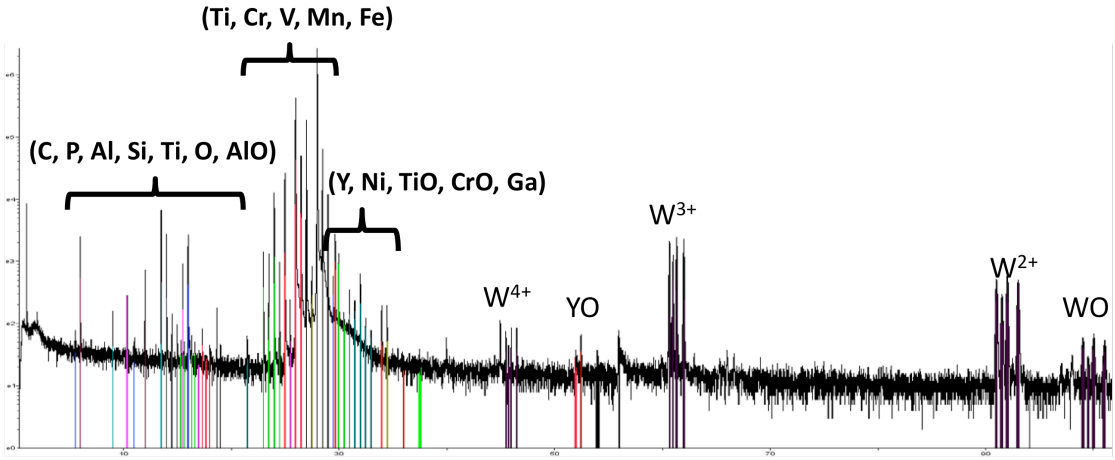

a

Figure 4.10. Composition and m/c spectrum of milled L2311S powder using improved attritor milling procedure.

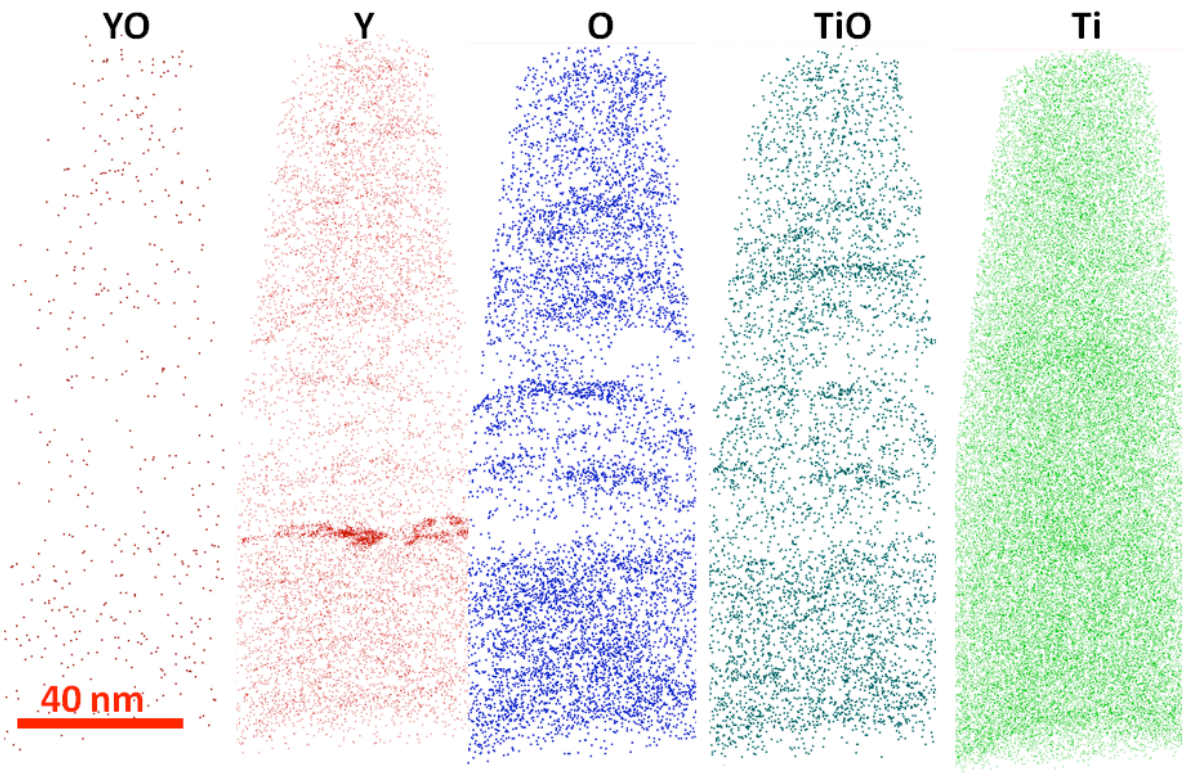

Figure 4.11. Atom maps showing solute segregation in milled L2311S powder using improved attritor milling procedure.

4.1.1.3 Grain structure

After annealing or HIP consolidation, all the powders and consolidated alloys contained bimodal grain size distributions; the smallest grain diameters were less than 1 µm while the largest were over 10 µm. The fraction of small grains depends on milling method and the final processing temperature. Examples of the grain structures for the Ar atomized powders attritor milled for 1, 5 and 20 h and then annealed (1150ºC, 3h), using the FIB are shown in Figure 4.12. The small grain volume fraction increased with longer milling times. A similar bimodal grain size distribution was observed in the SPEX milled and annealed (1100°C) powders. Previous research on NFAs composed of atomized metal-Y_2O_3 milled powders suggested that there are far fewer Ti, Y, and O-enriched NFs

in the larger micron-size grain regions, presumably due to low Y levels. In this case, however, NFs are present throughout the material, as discussed in section 4.1.2.

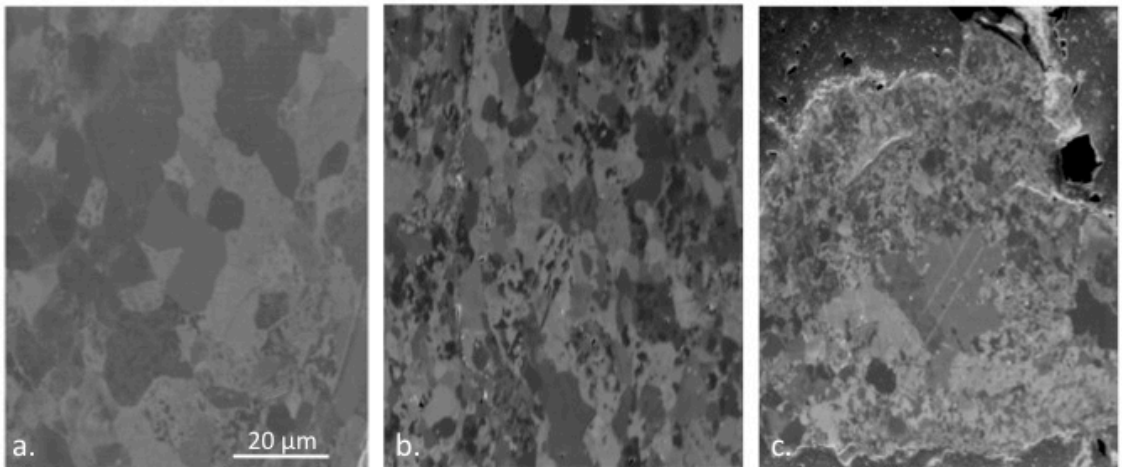

Figure 4.12. Grain structure of Ar atomized and annealed L2311M powder with attritor milling times of: a) 1 h; b) 5 h; and c) 20 h.

The grain structure in the consolidated OW1, OW3, and OW4 alloys was observed by optical microscopy of polished and etched surfaces. Example images are shown in Figure 4.13, and surprisingly, the small grain area fraction (f_s) varied significantly between each alloy. The first HIP consolidated alloy, OW1, had a small grain volume fraction of 70%. Alloy OW3, made from the larger batch L237BS powder with low O contents was almost exclusively composed of large grains with a small grain volume fraction of 2%. Alloy OW4, which was milled with FeO to increase the O content only also had a low f_s of ≈ 10%. The differences in the bimodal grain structure between OW1, OW3, and OW4 appear to be due to the effect of O content, as discussed in more detail is given in section 4.1.2.4.

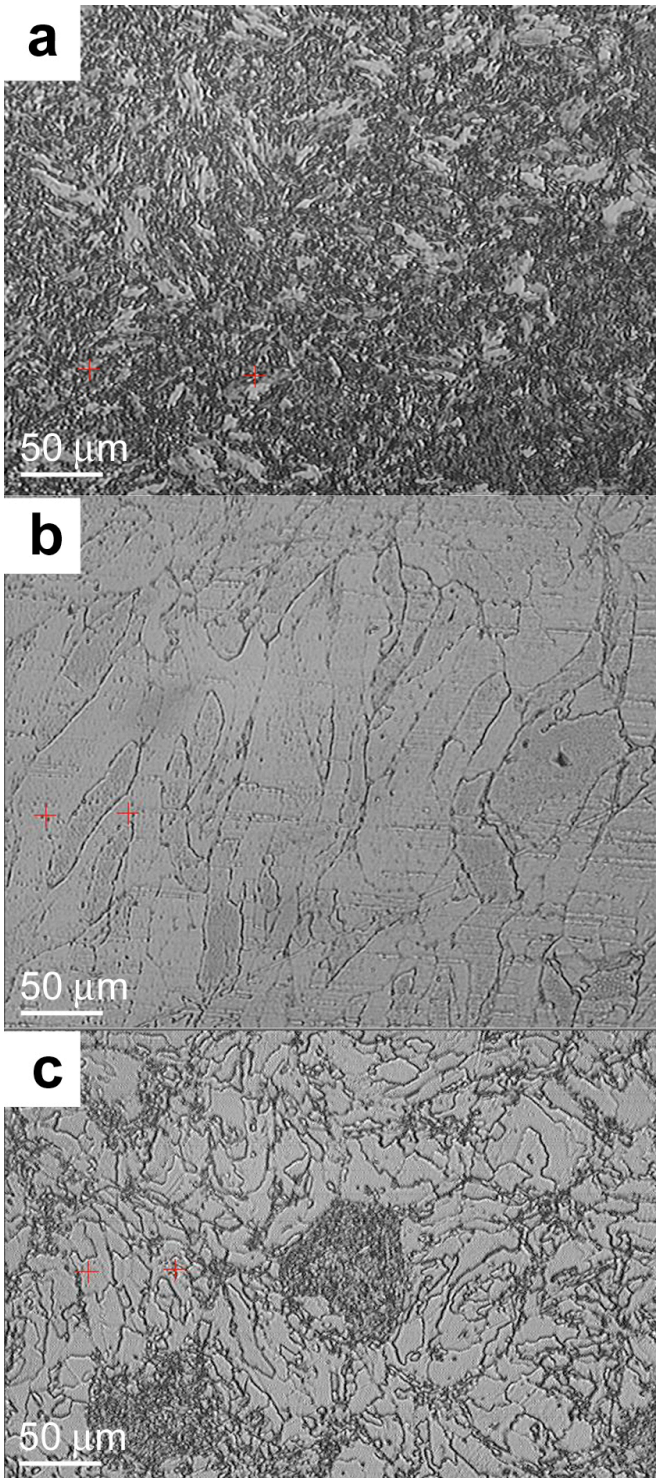

Figure 4.13. Optical micrographs of etched OWH (a); OWL (b); and OWI (c).

The final consolidated alloy produced was PM2 that was hot extruded at ORNL at 850ºC and annealed for 1 h at 1000ºC. This alloy was consolidated from the same powder milled with FeO as the OW4 alloy, but due to it's lower processing temperature was made entirely of fine grains. Figure 4.14 shows a BF TEM image of PM2 perpendicular to the extrusion direction.

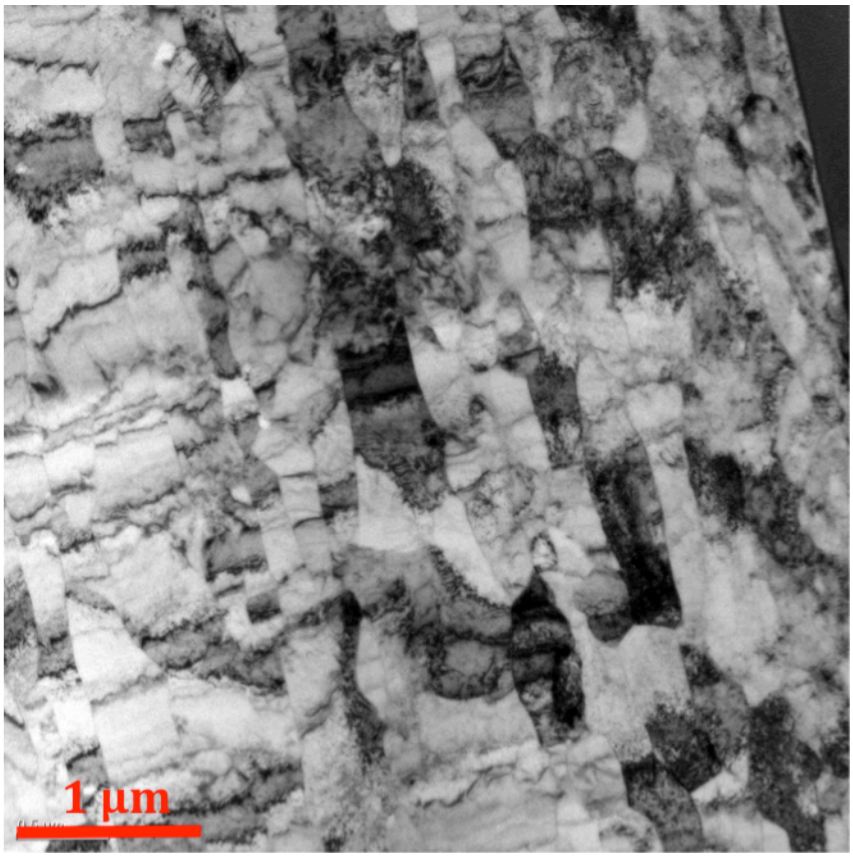

Figure 4.14. BSE SEM image of extruded alloy PM2.

4.1.2 NF characterization

The following sections summarize the results obtained for each of the NF characterization techniques used including SANS, TEM, and APT. The NFs were characterized after each processing step of atomization, ball milling and annealing or hot consolidation to compare the NF size, number density, volume fraction, and composition.

4.1.2.1 SANS

SANS measurements on many powders in various conditions and on the consolidated OW1, OW2, and OW3 alloys were carried out at the NIST Center for Neutron Research (Bethesda, MD). The as-atomized powders showed almost no additional scattering compared to a control powder atomized without Y, with the only difference occurring at low q values corresponding to larger features. Figure 4.15 shows example 45°±15° scattering curves for the Ar as-atomized powder (L2311S) and a control material with similar composition and processing but without Y. SANS measurements on the Ar/O and He atomized powders were similar.

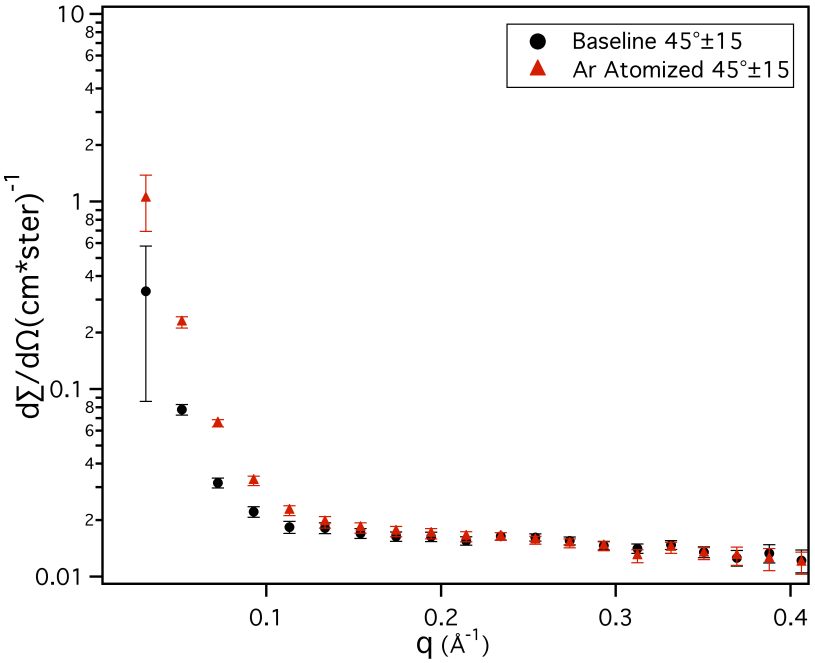

Figure 4.15. Example graph comparing Ar as-atomized powder with baseline Fe14Cr0.3W0.4Ti powder without Y.

Figure 4.16 shows the 45°, nuclear plus 0.5 magnetic scattering curves for the control specimen as well as the Ar, Ar/O and He atomized and SPEX milled (10 h) preliminary batch powders (L2311S, L2312S, and L2313S) annealed at 1100°C. The increased scattering at all q, especially between 0.1 and 0.3 Å^{-1}, signals the formation of NFs, and

shows that similar NFs were produced in all three atomization atmospheres. The NFs are also broadly similar to those observed in the NFA MA957 and other model 14YWT alloys produced by SPEX milled atomized metal alloy-Y_2O_3 powders and annealed or HIPed at 1150°C, although the M/N and f_v are somewhat higher in this case compared to the previous studies.

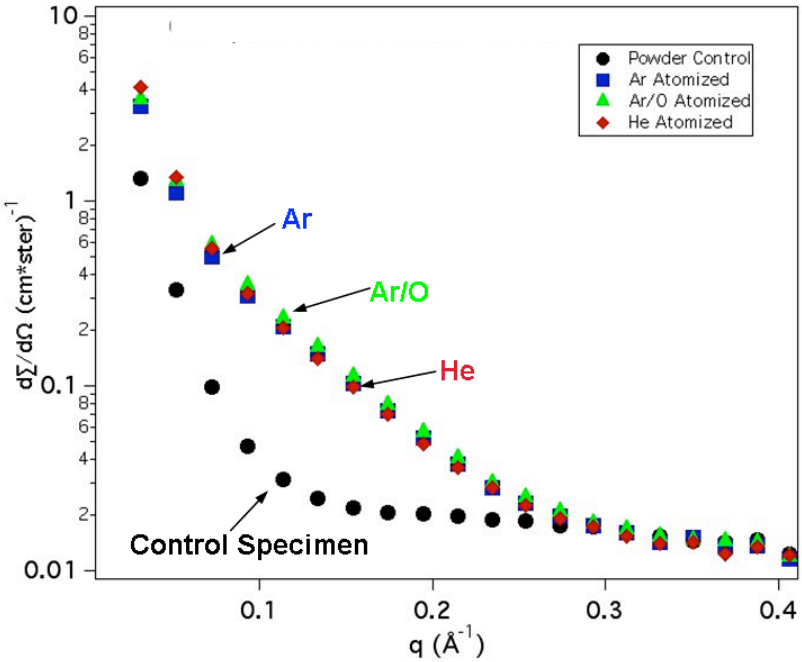

Figure 4.16. SANS 45° scattering curves comparing the Ar, Ar/O and He atomized, SPEX milled and annealed powders (L2311S, L2312S and L2313S).

Figure 4.17a shows that the scattering curves for the Ar/O atomized, medium sized (L2312M) attritor milled powders annealed at 1150°C systematically increase with milling times of 1, 5, 20, and 40 h. Similar results were observed for the L2311M powder milled for 1, 5, and 20 h and annealed at the same temperature. Figure 4.17b summarizes the average radius (<r>), number density (N) and volume fraction (f_v) of the precipitates characterized by SANS in this work. The Ar atomized powder (L2311M) that was attritor milled for 20 h contains an almost identical population of NFs as the 40 h Ar/O powder

(L2312M). The 20 h Ar/O powder has larger scattering features and lower N and f_v compared to the 20 h Ar powder, suggesting that the Ar/O powder requires longer milling times. The OW1 and OW2 alloys consolidated from the 40h Ar attritor milled powders have the smallest NFs and the highest N, and are comparable to the NFs in the 10 h SPEX milled powder (L2311S) annealed at 1100ºC. The NFs formed by the sequence of an isothermal anneal of OW2 powders at 1000ºC for 1 h prior to HIP consolidation at 1150°C were very similar to those in the OW1 alloy directly HIPed at 1150°C; the NF radius is slightly larger in the annealed and HIPed alloy ($\langle r \rangle \approx 1.44$ vs. 1.4 nm) and the number density is slightly lower ($N \approx 1.0$ vs. 1.1×10^{24} m^{-3}).

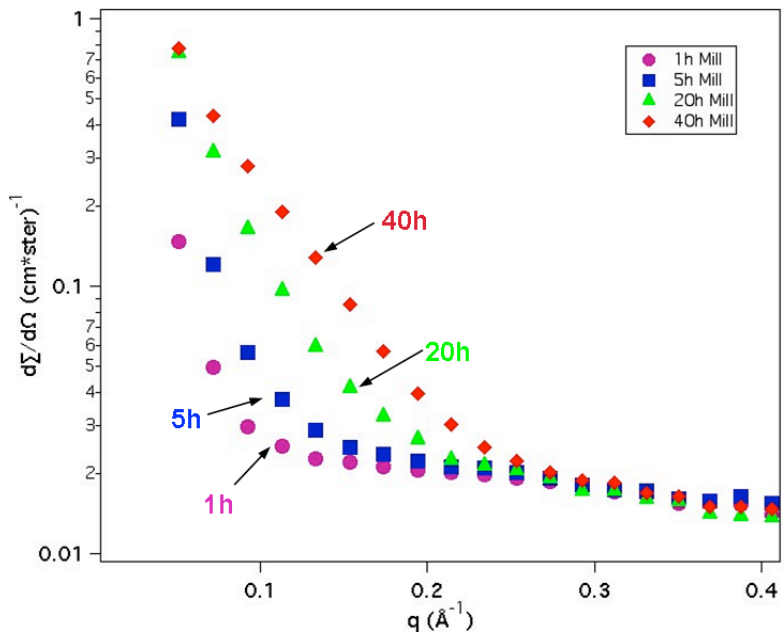

a

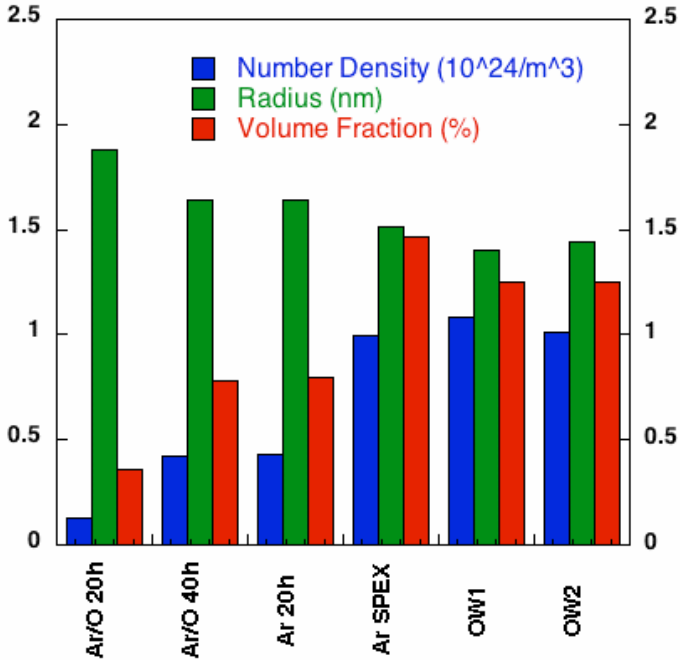

b

Figure 4.17. a) SANS 45° scattering curves comparing the Ar/O atomized, attritor milled and annealed powders (L2312M) for milling from 1 to 40 h and b) a comparison of the size, number density, and volume fraction of select 14YWT powders and alloys.

SANS was also performed on the consolidated alloy OW3 as well as several powders milled with FeO and ramp annealed at 850ºC, 1000ºC, 1150º and one isothermally annealed at 1150ºC. The powder annealed at 1150ºC has the most similar processing conditions to alloy OW4. Figure 4.18 shows the 45º scattering curve for a control alloy, OW1, OW3 and the 1150ºC annealed powder representative of OW4. Alloy OW2 had similar scattering to OW1, this is not included in Figure 4.18. Alloys OW1 and OW4 (powder equivalent) show the most scattering. Alloy OW3, with the lowest O content, shows the least scattering.

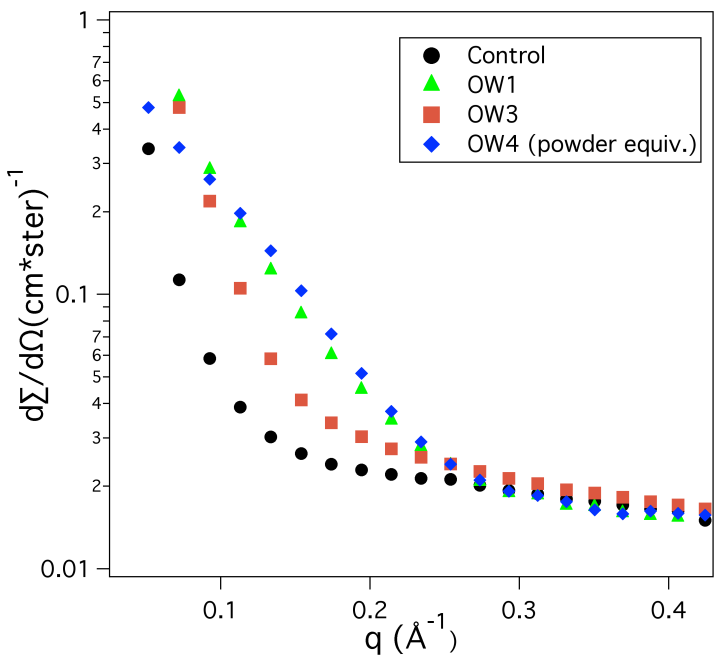

Figure 4.18. SANS 45° scattering curves comparing the OW1, OW3, and OW4 alloys.

Table 4.6 summarizes the average <r>, N, and f_v and M/N ratio for the NFs in all powders and consolidated alloys with sufficient scattering to perform the least square fitting. The SANS data reveals the NFs are broadly similar to those observed in MA957

and other model 14YWT alloys produced by mechanical alloying of Y_2O_3 with Fe alloy powders and annealing or HIPing at 1150°C [7,10].

Table 4.6. Summary of the SANS results.

Material	Description	<r> (nm)	M/N	N ($10^{23}/m^3$)	f_v (%)
SPEX Milled Powders					
Ar	10 h SPEX 1100ºC ann.	1.51	2.3	9.9	1.5
Ar/O	10 h SPEX 1100ºC ann.	1.51	2.3	11.0	1.7
He	10 h SPEX 1100ºC ann.	1.53	2.5	9.4	1.5
Attritor Milled Powders					
Ar	20 h milled/1150ºC ann.	1.66	1.4	4.2	0.8
Ar/O	20 h milled/1150ºC ann.	1.86	1.7	1.4	0.4
Ar/O	40 h milled/1150ºC ann.	1.64	1.2	4.3	0.8
Ar	40 h milled with FeO/1150ºC (OW4)	1.40	1.2	7.1	0.8
Ar	40 h milled with FeO/1000ºC ann.	1.23	1.1	12.5	1.0
Ar	40 h milled with FeO/850ºC ann.	1.07	1.1	23.4	1.2
Ar	40 h milled with FeO/iso1150ºC ann.	1.41	1.2	7.2	0.9
HIP Consolidated Alloys					
OW1	Ar atomized 40 h mill	1.40	2.4	11.0	1.2
OW2	Ar atomized 40 h pre-anneal 1000ºC	1.44	2.3	10.0	1.3
OW3	Ar atomized 40 h mill low O	2.70	1.1	0.5	0.4

Both the SPEX milled powders and the OW1 and OW2 HIP consolidated alloys have high M/N (>2), N and f_v, consistent with previous SANS studies on 14YWT alloys [10]. However, the M/N for attritor-milled powders were consistently lower ranging from ≈ 1.1 to 1.7 and averaging ≈ 1.3 with standard deviation of ±0.2. This range is similar to that observed in MA957 where the French alloy is ≈ 1.1±0.1 and the US alloy is ≈ 1.9±0.1. Note the 1 and 5 h attritor milled and annealed powder results are excluded from Table 4.6 because there was much less scattering in these cases indicating insufficient Y mixing. The M/N ratio is nominally controlled by the NF composition and atomic density. However, the measured M/N also may be affected by the fidelity of the control sample and if the magnetic field strength if the alloy is not fully saturated. The f_v in the SPEX milled powder and the OW1 and OW2 consolidated alloys is larger than can be

accounted for by all the Y, Ti and O solutes in the form of $Y_2Ti_2O_7$ or Y_2TiO_5 phases ($f_v \approx 0.8$), indicating the NF composition is non-stoichiometric, or there are additional scattering features. The attritor milled and 1150ºC annealed powders have lower f_v and M/N that are more consistent with the complex oxides. Note that using a measured M/N that is larger than the actual value leads to a modest overestimate of f_v; however, even assuming large errors in the measured M/N, this effect is not sufficient to result in large artificial increase in f_v.

Other trends that are shown in Table 4.6 include.

- The <r> are smaller and N larger in the Ar atomized powder attritor milled for 40 h with FeO, compared to both the Ar atomized powders milled for 20 h and the Ar/O powders milled for 40 h which gain O during processing; however the f_v are similar.
- The <r> and f_v increase and N decreases with increasing annealing temperature, while the M/N remained similar, consistent with previous observations [10].
- The <r> are lager and N and fv smaller in the OW3 alloy with low O. The effect of O is discussed further in section 4.1.2.4.

4.1.2.2 TEM

TEM characterization was carried out mostly on FIB lift-out specimens taken from several of the milled and annealed powders and consolidated alloys. The FIB lift-out specimens were ≈ 10 μm long, 5 μm wide, and less than 100 nm thick. Both twinjet electropolishing and extraction replicas were also prepared on selected consolidated alloys.

No large, Y-rich precipitates were found in the Ar atomized (L2311S) SPEX milled and annealed powder, but a high number density of NFs were present. The Ar atomized (L2311M) 40 h attitor milled and annealed powder contained several faceted 10 and 20 nm Y-rich precipitates as shown in Figure 4.19a, along with a high density of Y-Ti-O NFs. Many small NFs were also observed in the Ar/O (L2312M) milled and annealed powder, shown in Figure 4.19b. A clear picture of the NF population comparing the large and small grains was not possible due to the small size of the FIB lift-out specimens.

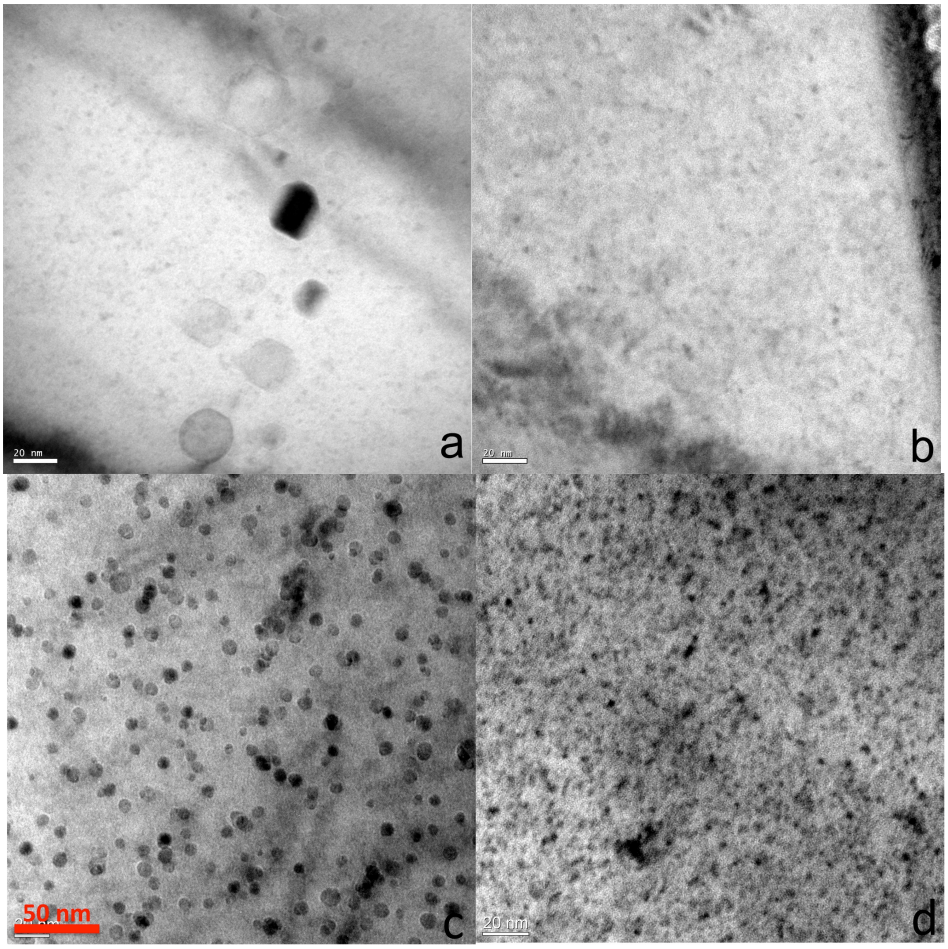

Figure 4.19. Bright field TEM images showing some large Y rich precipitates and numerous NFs in 40 h attritor milled and annealed a) Ar (L2311M); and b) Ar/O (L2312M) powders; c) L237BS milled and annealed powder with larger precipitates; and d) L2311M powder milled with FeO and annealed showing high density of small NFs.

Table 4.7 summarizes the milled and annealed powder results. The average NF diameter (<d>) measured by TEM ranged from 2.7 nm to 3.2 nm in all of the milled and annealed powders except the Ar atomized (L237BS) 40 h milled powder that used the improved attritor milling procedure, resulting in a low O content, with <d> ≈ 6.3 nm in diameter. An example TEM image of the L237BS powder is shown in Figure 4.19c. EDX showed the larger precipitates in the low O case typically had high Y/Ti ratios >> 1. The corresponding N ≈ $0.4x10^{23}m^{-3}$ and f_v ≈ 0.52% were lower compared to the average N ≈ $1.9x10^{23}m^{-3}$ and f_v ≈ 0.24 % for powders and alloys with higher O, including for the case of milling with FeO as seen in Figure 4.19d.

Table 4.7. Average diameter, number density, and Y/Ti ratios of 14YWT annealed powders.

NF parameters	**Ar-40h Attritor**	**Ar/O-40h Attritor**	**Ar-low contamination**	**Ar-40h w/FeO**
<d> (nm)	2.7	3.2	6.3	2.8
N (10^{23} m^{-3})	2.0	1.6	0.4	2.1
f_v	0.21	0.27	0.52	0.24
Y/Ti	0.8	-	>> 1	0.74

TEM specimens of the OW1 and OW2 HIP consolidated alloys were prepared by twinjet electropolishing allowing a larger area of material to be imaged. Figure 4.20a and b show the bimodal grain size distributions in both alloys. The large grains are on the order of several μm and the small grains are between 20 and 500 nm. The higher resolution micrographs in Figure 4.20c and d show that there are also numerous NFs in the large grain regions of both OW1 (Figure 4.20c) and OW2 (Figure 4.20d). The in-foil N/<d> for the OW1 and OW2 were $1.2x10^{23}m^{-3}$/3.4 nm and $1.7x10^{23}m^{-3}$/2.6 nm, respectively.

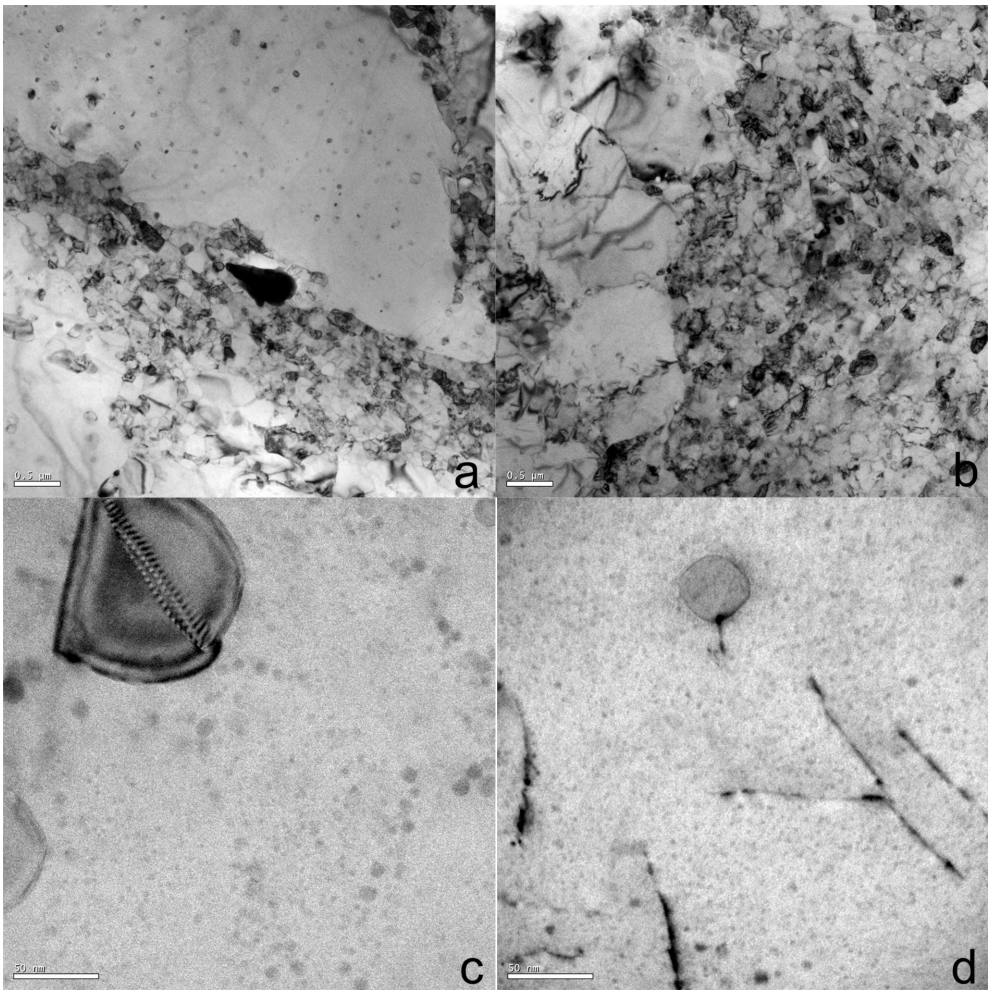

Figure 4.20. Low magnification TEM images show grain structure in a) OW1 and b) OW2, respectively. Higher magnification TEM images show NFs in the large grains for both c) OW1 and d) OW2.

HRTEM was carried out on extracted NFs to investigate their crystal structures. Several NFs were observed from OW1, but none of the resulting FFT diffraction patterns or measured lattice spacings were consistent with known Y-Ti-O structures. However, several NFs in OW2 had a cubic structure and lattice spacing consistent with pyrochlore $Y_2Ti_2O_7$, which was also observed in MA957 [22]. Figure 4.21 shows bright field and HRTEM images of NFs in OW2 where the measured interplanar angles and lattice spacing indicates a cubic structure. Extraction replica samples were also prepared from

alloy OW3, but the precipitates could not be identified with any known Y-Ti-O structure and the Y/Ti ratio was much larger than 1.

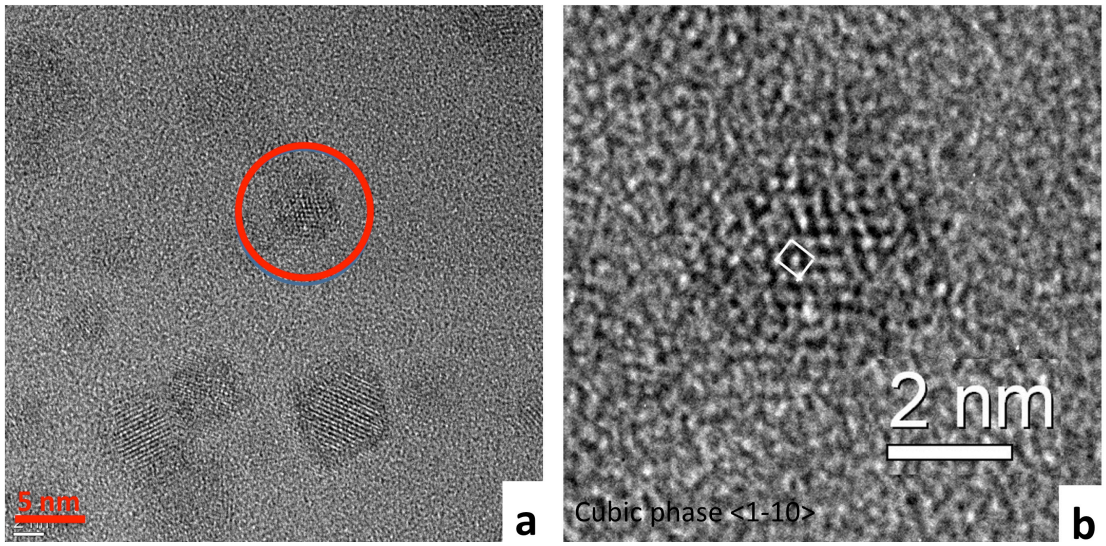

Figure 4.21. Alloy OW2 a) bright field TEM image of NFs in extraction replica sample; and b) HRTEM image of single NF < 5 nm in diameter.

HIP consolidated alloys OW1, OW3, and OW4 permitting a systematic study of how O affects the NFs at high, low, and medium levels, respectively. Additional TEM results are presented in section 4.1.2.4. A summary of the <d>, N and f_v measurements for all consolidated alloys are given in Table 4.8.

Table 4.8. The <d>, N, f_v and Y/Ti ratios of 14YWT consolidated alloys.

NF parameters	OW1	OW2	OW3	OW4	PM2
<d> (nm)	3.4	2.6	4.7	2.4	1.4
N (10^{23} m^{-3})	1.2	1.7	0.6	2.8	5.2
f_v	0.25	0.16	0.33	0.20	0.07
Y/Ti	1.2	0.9	>> 1	0.5	< 1 TBD

The final alloy characterized in this study, designated as PM2, was produced at ORNL by milling the as-atomized powders with FeO followed by hot extrusion at 850°C, annealing for 1 h at 1000°C, and cross rolling to 50% thickness. PM2 had the highest N ≈ 5.2×10^{23} m^{-3} and smallest <d> ≈ 1.4 nm NFs among the five consolidated alloys observed

by TEM. EDX in-foil measurements showed the NFs to have Y/Ti that are typically less than 1.

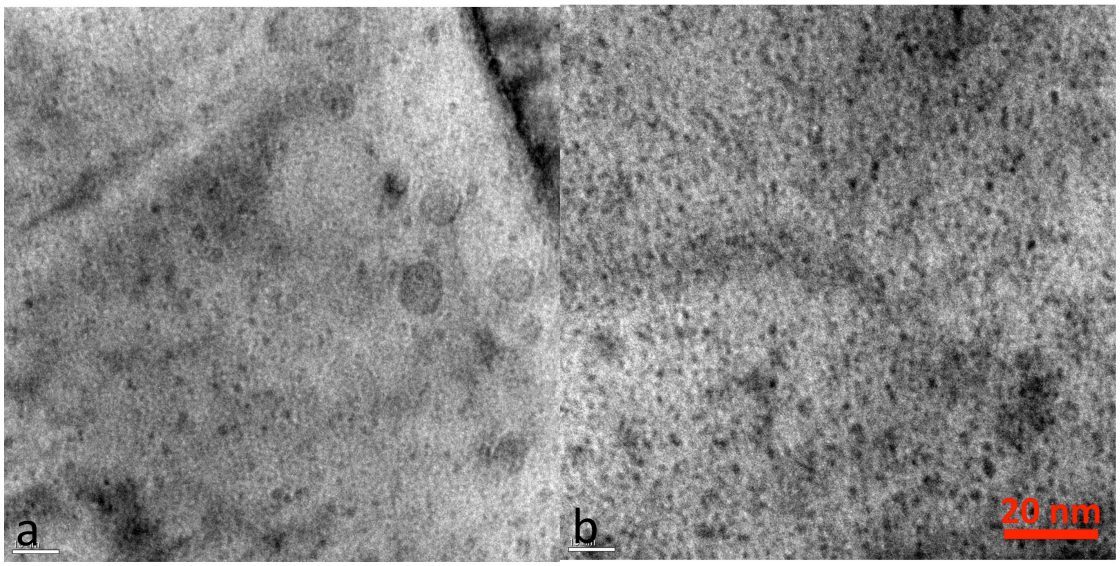

Figure 4.22. Bright field TEM images of extruded and cross-rolled PM2 alloy.

4.1.2.3 APT

APT was carried out on the Ar atomized small and medium sized powders (L2311S and L2311M) in the 10 h SPEX and 20 h and 40 h attritor milled and annealed conditions. FIB lift-outs were taken from both large and small grains in the SPEX milled and annealed powder (see below). APT was also used to characterize the OW1, OW2, OW3, OW4, and PM2 consolidated alloys.

A high concentration of NFs were observed in 10 h SPEX milled L2311S powders annealed at 1100°C in both large and small grains. Figure 4.23 shows an atom map in a small grain region (13 million ions) with a high density of NFs. The NFs are larger on the grain boundaries, which are also marked by phosphorus segregation.

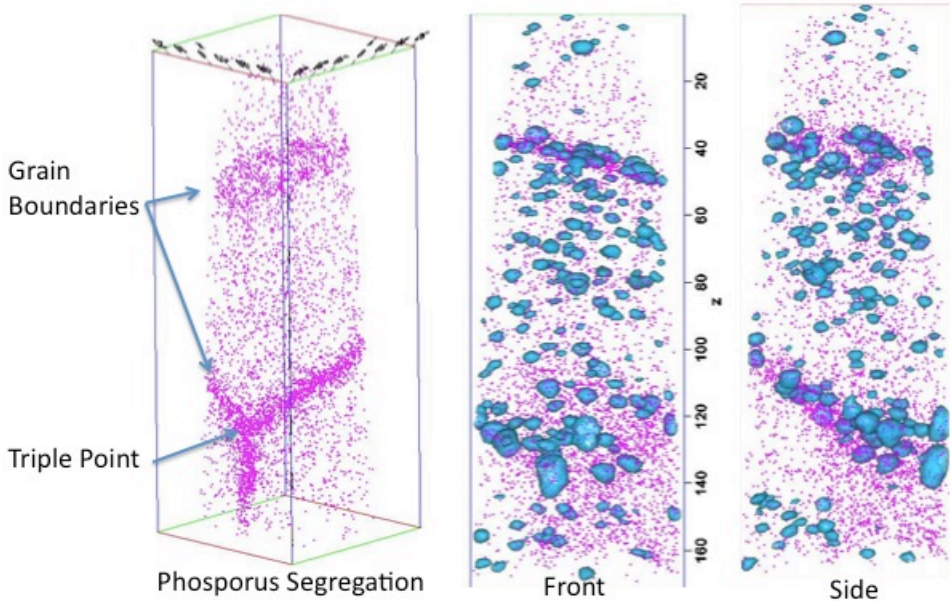

Figure 4.23. An APT atom map reconstruction of a small grain region in the 10 h SPEX milled and annealed Ar atomized powder (L2311S) showing phosphorus segregation to grain boundaries and Y-Ti-O iso-density surfaces (0.9 atom/nm^3) for the NFs.

As illustrated in Figure 4.24a, the FIB was used to select an APT needle lift-out region from a large grain area. Platinum strips were randomly deposited on the polished particle surface to protect the substrate from Ga ion bombardment that was then used for ion etching the grain structure to observe in the SEM. The Y-Ti-O isoconcentration surfaces in Figure 4.24b (39 million ions) show a high number density of precipitates in the large grain region. This is not consistent with some previous research (and intuition) that postulated that large grains are associated with regions containing a low number density of NFs. However, other studies have found NF in the larger grains [23]. Indeed, in this particular case the average N was higher in the large (7.5×10^{23} m^{-3}) compared to the small (3.4×10^{23} m^{-3}) grain regions. However, given the sample-to-sample and grain-to-grain variations no general conclusion can be drawn from this numerical comparison.

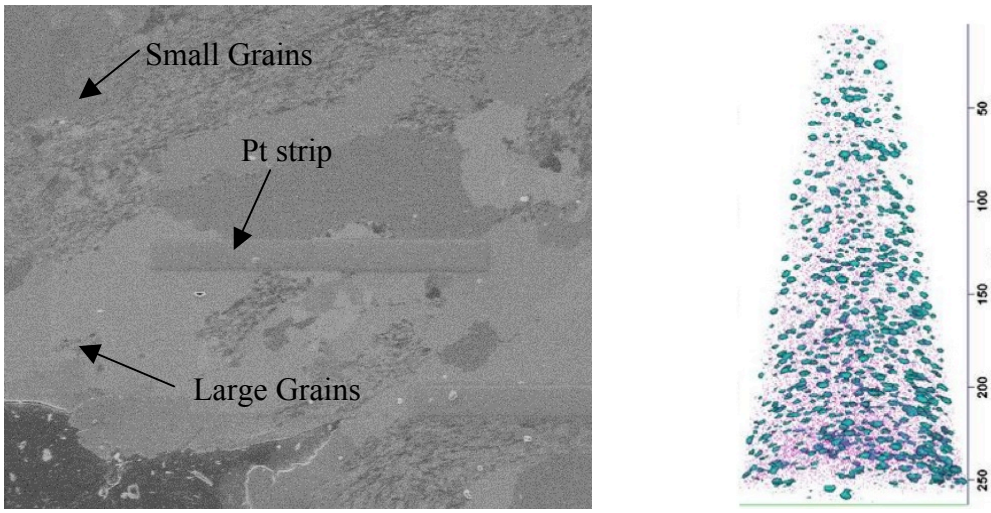

(a) (b)

Figure 4.24. a) A dual-beam FIB image of bimodal grain distribution in a 10h SPEX milled Ar atomized and annealed L2311S powder showing the Pt masked FIB lift-out area; b) Y-Ti-O iso-density surfaces (2 atom/nm^3) in blue showing NFs in large grain region.

As reported previously, a standard IVAS analysis of the APT data indicates that the NFs contain a significant amount of matrix Fe (≈ 50-70 %) and Cr. However this is an artifact caused by trajectory aberrations. Excluding the matrix Fe and Cr and focusing on the Y/Ti/O ratio compositions in the SPEX milled alloy L2311S powders gives Y/Ti/O ratios of 30/30/40 for the small grain area and 26/33/41 for the large grain area, respectively. APT on the Ar atomized 40h attritor milled powder showed similar results as to the SPEX milled powder. The Y/Ti ratios are much higher than observed in MA957 and are more consistent with $Y_2Ti_2O_7$. Note these 14YWT contain less Ti (0.4 wt.%) than MA957 (1.0 wt.%).

The 20 h and 40 h attritor milled and annealed Ar atomized L2311M powders were also characterized using APT. Small Y-Ti-O precipitates are observed in both cases. The TiN and WN peaks in the mass spectrum increased with the milling time between 20 and 40 h consistent with increasing N impurity pickup. Table 4.9 shows the average bulk

powder composition for two volumes (2.2 and 8.2 million ions) for the 40 h ball milled powders. Note that both the Ti and Y values are low compared to the nominal alloy composition. One plausible explanation is that these elements were removed from solution by precipitation in nearby, but un-probed, volumes.

Table 4.9. The average APT composition of the attritor milled and annealed L2311M powder.

at.%	Fe	Cr	W	Ti	Y	O	C	N	Al	Si
	83.0	15.5	0.77	0.17	0.064	0.160	0.007	0.060	0.002	0.070

APT reconstructions of the 40 h attritor milled and annealed, Ar atomized L2311M powders exhibit a high number density of non-homogeneously distributed NFs, both in the matrix and on grain boundaries. The average NF N in the 40 h attritor milled powders is ≈ $3.0\pm0.4\times10^{23}$ m^{-3} and their <d> are ≈ 2.4 nm and 3.1 nm in the matrix and on grain boundaries, respectively. Table 4.10 shows the average composition of the NFs, again indicating a nominally high content of Fe (≈ 72 at.%). The corresponding average Y/Ti/O ratio is 25/35/40. An approximately 4 nm wide region of W, Ti, Cr, N, O and P segregation was also observed at the grain boundaries.

Table 4.10. The average APT composition of the NFs in the 40 h attritor milled and annealed L2311M powder.

at.%	Fe	Cr	W	Ti	Y	O	C	N	Al	Si
	72.6	17.8	0.80	3.07	1.91	2.93	0.01	0.65	0.07	0.17

Table 4.11 shows the APT compositions of two volumes (17.7 million ions) in the HIP consolidated OW1 alloy. Note the very high Ti, N and O concentrations in volume 1, versus much lower concentrations in volume 2. The excess Ti, N and O in volume 1 are

due to the presence of a large Ti-nitride phase shown in Figure 4.25. The Ti-nitride phase composition was shown previously in Table 4.4. The Ti concentration is about 55 at.%. N, Si and O concentrations are 15.3, 3.6 and 3.6 at.%, respectively. Figure 4.25 also shows a lower density of NFs around the grain boundary, which is also typical in these alloys.

Table 4.11. The APT compositions of two volumes from OW1 alloy

at.%	Fe	Cr	W	Ti	Y	O	C	N	Al	Si
Vol. 1	72.4	14.2	0.91	6.4	0.08	0.82	0.07	4.48	0.005	0.50
Vol. 2	83.7	14.5	1.0	0.17	0.09	0.04	0.09	0.14	0.011	0.18

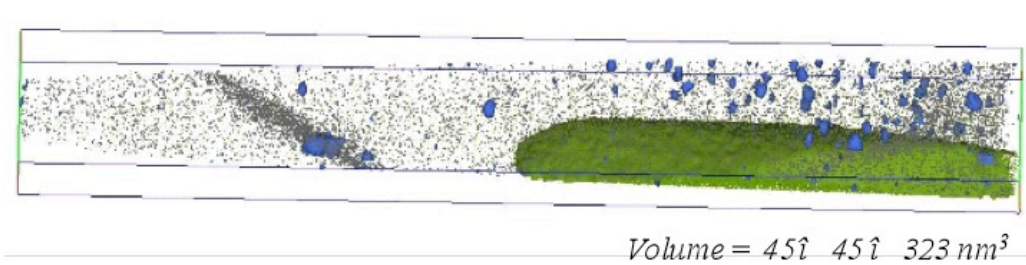

Figure 4.25. An APT reconstruction of a volume in the OW1 alloy. C atoms (grey) are segregated at a grain boundary. Iso-concentration surfaces (11%) for TiN ions are shown in green and for Y+YO ions (1%) from the NFs are shown in blue.

As in the case of the annealed powders, the OW1 alloy contains a heterogeneous distribution of NFs along with some larger NFs on the grain boundaries. The average NF N ≈ 3.0±0.4x10^{23} m^{-3}, and the average diameter is ≈ 1.7 nm for NFs in the matrix and 2.3 nm on the grain boundaries. The average composition of NFs is given in Table 4.12, and the corresponding Y/Ti/O ratio is 22/37/41. As observed in the ball milled and annealed powders, W, Ti, Cr, N, O and P segregate to the grain boundaries in OW1 over a region 5 nm wide.

Table 4.12. The average APT NF composition in the OW1 alloy.

at.%	Fe	Cr	W	Ti	Y	O	C	N	Al	Si
	60.3	21.8	0.97	5.3	3.1	5.8	0.10	1.70	0.07	0.53

Table 4.13 shows the average APT compositions of three volumes (23 million ions) in the HIP consolidated OW2 alloy. The Ti concentration is again low and the Y and O concentrations are about 2/3 of the expected bulk composition.

Table 4.13. The average APT composition for three volumes in the OW2 alloy.

at.%	Fe	Cr	W	Ti	Y	O	C	N	P	Si
	84.2	13.7	0.99	0.13	0.08	0.36	0.03	0.12	0.03	0.13

As shown in Figure 4.26, the distribution of NFs appears to be more homogeneous in the OW2 alloy compared to both the OW1 alloy and the small grain area in the Ar/0 atomized (L2312S) milled and annealed powder. Note OW2 was pre-annealed at 1000°C before receiving the standard HIP consolidation treatment at 1150°C. The average NF density in the OW2 alloy is ≈ 6.7±0.4x1023 m^{-3} and the <d> ≈ 2.1 nm. The average composition of the NFs is shown in

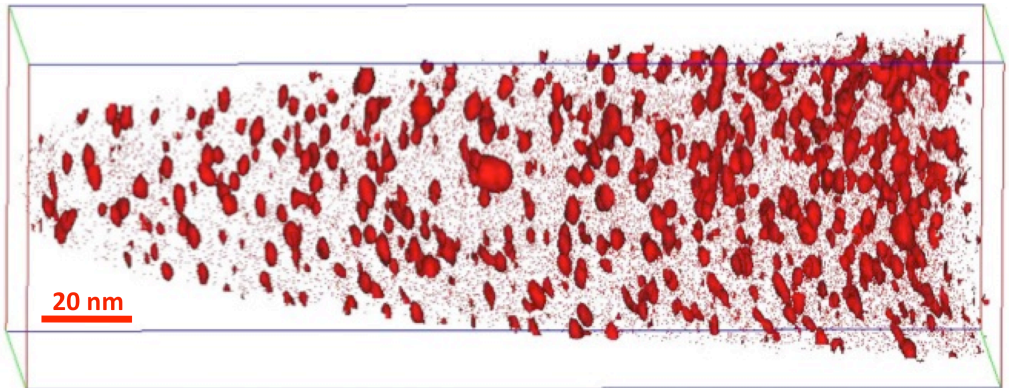

Figure 4.26. An APT reconstruction of a volume of OW2 analyzed by APT. The NFs are shown Ti by TiO and YO iso-composition surfaces (0.9 at%).

Table 4.14. The average APT NF composition in the OW2 alloy.

at.%	Fe	Cr	W	Ti	Y	O	C	N	Al	Si
	70.0	20.2	0.87	2.21	1.72	3.7	0.06	0.20	0.03	0.48

Figure 4.27 compares the N and <d> of NFs in the 40h attritor milled and annealed Ar atomized L2311M powder, OW1 and OW2. Figure 24 shows the corresponding plot of the size distribution of the NFs, While they are generally similar, the pre-annealed OW2 alloy has the highest number density of NFs. The hardness of the alloys is similar at 429±12 for OW2 and 443±14 for OW1.

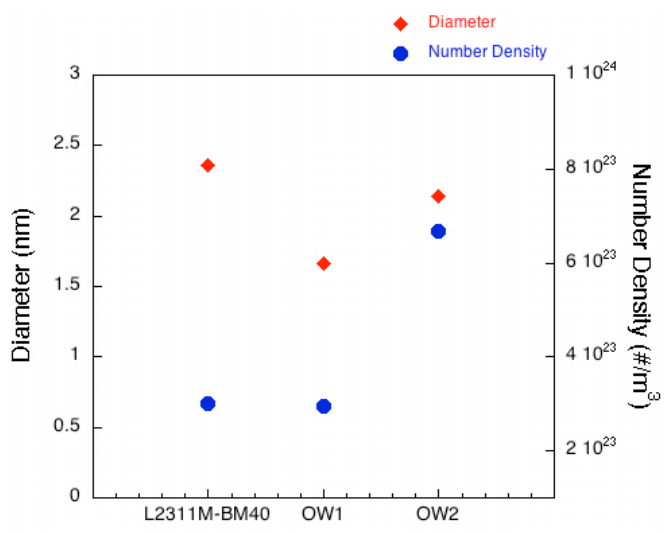

Figure 4.27. Comparison of the number density and the average diameter of NFs in the Ar atomized, 40 h attritor milled and annealed powder (L2311M) and OW1 and OW2 alloys.

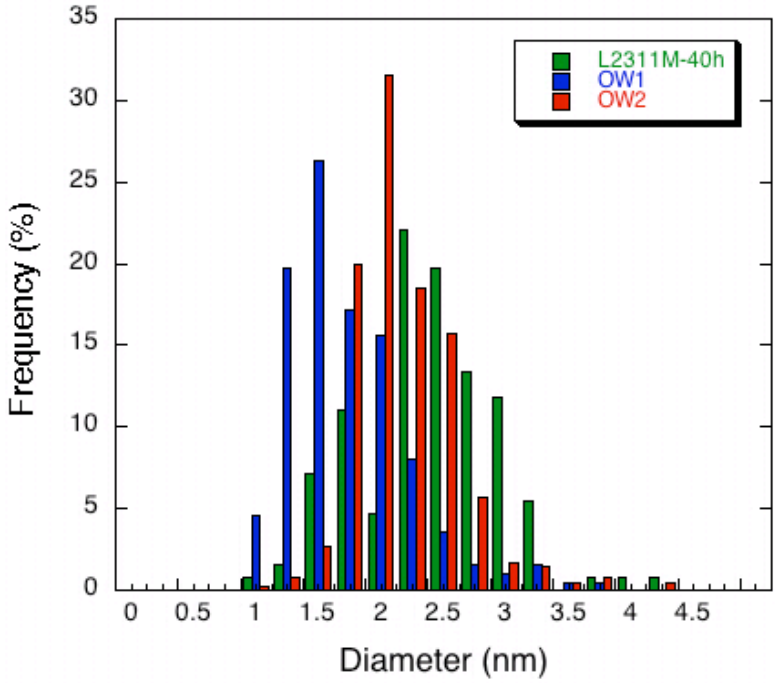

Figure 4.28. Comparison of the size distribution of NFs in the L2311S powder, OW1 and OW2 measured by APT.

The APT results indicate that small NFs are present in both large and small grains. The NF number densities, diameters and compositions are roughly similar in all the powder and consolidated conditions examined. Again the larger precipitates are associated with the grain boundaries. Perhaps the most significant difference between the various conditions was the NF Y/Ti ratio, which ranged from a high of 0.85 for the SPEX milled powder to a low of 0.57 for the OW1 alloy. Major differences in the NFs were observed in the OW3 and OW4 alloys compared to the powders and alloys with higher O and N contamination. The next section describes in detail the differences between these alloys due to the O content.

4.1.2.4 Oxygen effects

Ukai has previously noted the importance of O content on the formation of the NFs [25]. The alloys OW1, OW3, and OW4, were useful in exploring the effects of O on the

microstructure and NFs. For clarity, the alloys are referred to here as OWL (OW3), OWI (OW4), and OWH (OW1) to indicate low, intermediate, and high O contents. Examining the micro-nanostructure and hardness of the three alloys provides an opportunity to assess the effects of O in a fully ferritic 14CrYWT alloy. The drastic effect O has on the NFs is readily apparent by the atom map and TEM micrographs in Figure 4.29a and b, showing much larger precipitates in OW3 than in the OW1 and OW2 alloys (see Figure 4.20 and Figure 4.26).

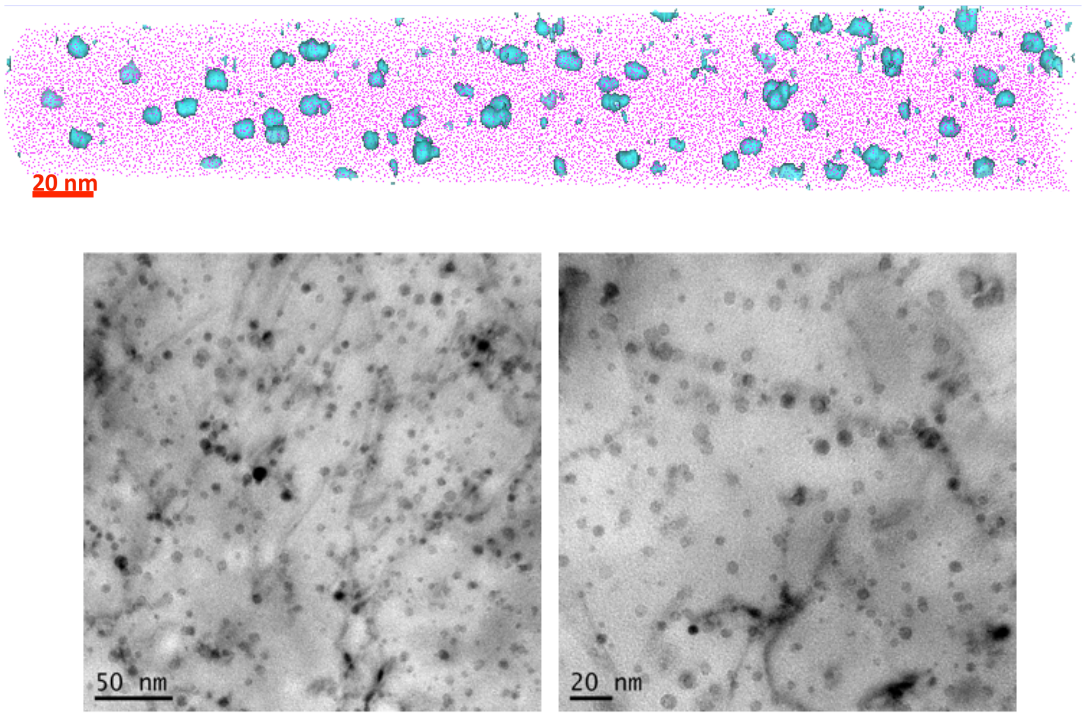

Figure 4.29. a) An APT reconstruction of a volume in the OWL alloy showing a lower density of larger NFs compared to the results for the preliminary batches of powders (Y isoconcentraition = 0.5%); b) Bright field TEM micrographs showing NFs in OWL alloy.

Table 4.2 shows the O and N contents (wt.%) of the three powders after milling measured by inert gas fusion. All three alloys were HIP consolidated at 1150ºC at 200 MPa for 3 h.

Table 4.15. O and N content (wt.%) for OWL, OWI, and OWH alloys

Alloy	**O (wt.%)**	**N (wt.%)**
OWH	0.249	0.190
OWI	0.127	0.013
OWL	0.065	0.016

As shown previously in Figure 4.13, all three alloys have a bimodal distribution of large grains, up to many tens of μm in OWL, and small, < 1 μm, grains. Table 4.17 summarizes the grain structures, characterized by the two average large and small grain sizes (d_s, d_l) and the relative fraction of the small grains (f_s). The d_l increased (9.5 μm to 23.3 μm) and the f_s decreased (70% to 2%) systematically with decreasing O content. The smallest d_s (0.151 μm) was observed in the highest O content (OWH) alloy. However, systematic ordering of d_s is not observed in the intermediate and low O content alloys (OWI and OWL).

The typical TEM micrographs in Figure 4.30 show the NFs in OWH, OWI and OWL. The NF size distributions are compared in Figure 4.31. The average NF <d> and number N in the low O (OWL), intermediate O (OWI) and high O (OWH) content alloys measured by TEM are summarized in Table 4.17. Clearly, the NFs in the low O content alloy are coarser and fewer than those in intermediate and high O content alloys. The NFs in OWH are only slightly larger with a lower number density than those in OWI.

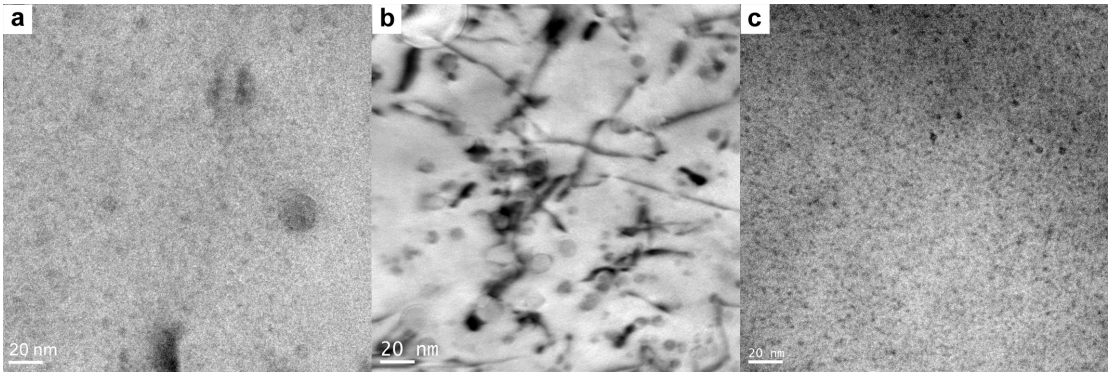

Figure 4.30. TEM micrographs of the NFs in OWH (a); OWL (b); and OWI (c).

Energy dispersive X-ray spectroscopy (EDX) measurements were used to estimate the compositions of NFs extracted on C foils. In OWL, 15 out of the 20 observed precipitates were Y-rich and contained no Ti (average diameter ≈ 7.0 nm), while one had a Y/Ti ratio of ≈ 1.5 (diameter ≈ 12.0 nm) and 4 had Y/Ti ratios between 2 and 10, averaging 4.6 (average diameter ≈ 6.0 nm). In contrast, the average Y/Ti ratio was 0.5 (d < 10 nm) in OWI and 1.2 (d < 5 nm) and 2.3 (5 < d < 10 nm) in the OWH.

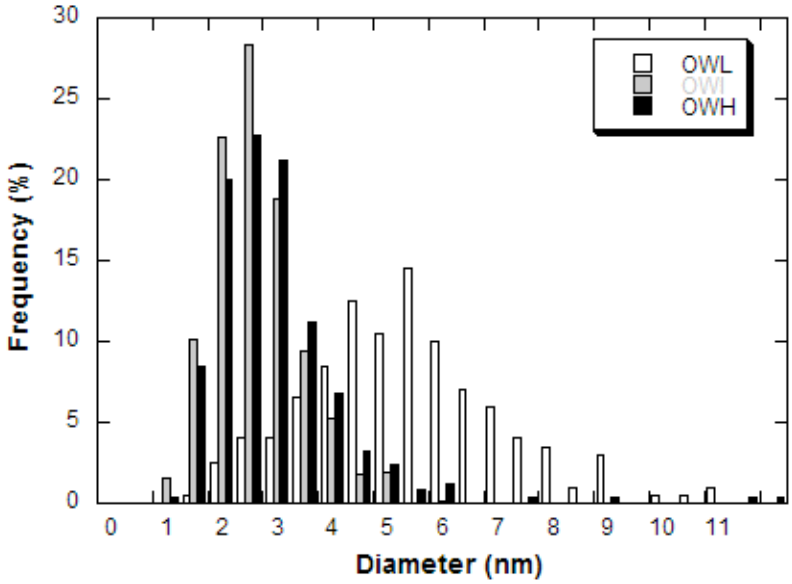

Figure 4.31. Size distributions of the NFs in OWH, OWL and OWI measured by BF TEM.

Figure 4.32 shows representative APT NFs for OWH, OWI and OWL. The corresponding alloy and NF compositions are shown in Table 4.17. The OWL had the largest <d> and lowest N, with <d> = 5.8 nm and N = $6.0\times10^{22}/m^3$, in contrast to smaller diameters of 1.7 nm and 2.5 nm and higher N of $2.9\times10^{23}/m^3$ and $9.6\times10^{23}/m^3$ for OWH and OWI, respectively. The APT Y/Ti/O ratios for OWH, OWI, and OWL are 23/37/41, 11/42/47 and 22/31/46, respectively. OWL has the highest Y/Ti ratio, but it is still less than 1, which is inconsistent with the TEM extraction replica results. The average APT alloy NF composition shown in Table 4.16 for OWL is similar to the OWH (OW1) and OW2 alloys with slightly lower Y and O content. The NF composition for this dataset is also given in Table 4.16.

Table 4.16. The average APT NF composition in the OWH, OWI and OWL alloys.

at.%	Fe	Cr	W	Ti	Y	O	P	Al	Si
Bulk	83.45	15.6	0.41	0.27	0.02	0.04	0.01	0.06	0.06
OWH NF	60.31	21.80	0.97	5.30	3.10	5.80	0.08	0.07	0.53
OWI NF	74.35	16.63	1.09	3.08	0.84	3.50	0.05	0.11	0.16
OWL NF	80.23	15.50	0.53	0.98	0.69	1.45	0.36	0.60	0.09

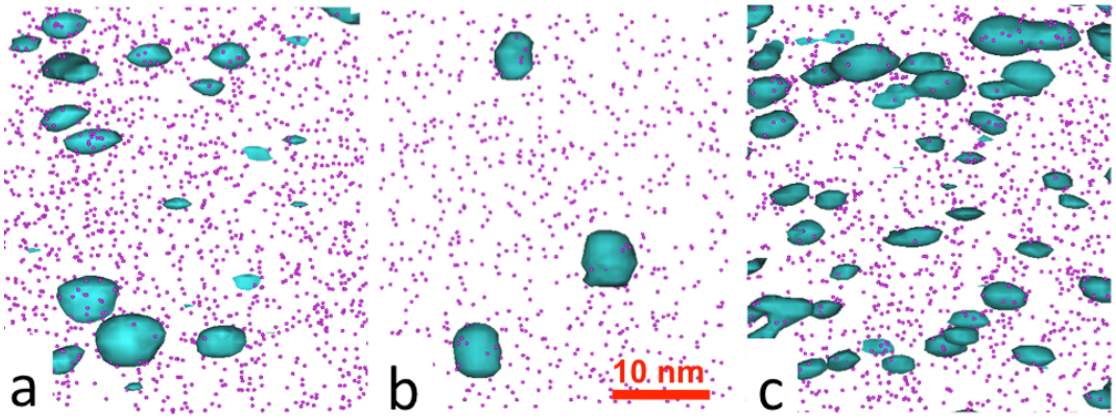

Figure 4.32. Twenty nm thick Atom maps with Cr ions and Y-Ti-O isoconcentration surfaces (4.0%) for (a) OWH, (b) OWL, and (c) OWI.

SANS was performed on OWH, OWL, and on an L2311M powder attritor milled with FeO and annealed for 3 h at 1150ºC, as a surrogate for the HIPed OWI. The SANS results are summarized in Table 4.17. The OWH alloy and the OWI surrogate powder both had smaller NF <d> compared to OWL and high N of $1.1\times10^{24}/m^3$ (OWH) and $7.1\times10^{23}/m^3$ (OWI). Consistent with the TEM and APT results, the low O content alloy, OWL has a much lower N ≈ $5.2\times10^{22}/m^3$. The nominal NF f_v are summarized in Table 4.17, for the OWH, OWI (surrogate) and OWL and were 1.2, 0.8 and 0.4% respectively. The NF f_v increased with increasing O content. The data in Table 4.17 also shows that the microhardness (H_v) increases with increasing O content.

With the exception of the smaller APT value of <d> for OWH, the sizes of the NFs are similar for the different characterization methods. There is a larger variation in N, with SANS and APT tending to give higher values compared to TEM. However, given both the limitations of the various methods and inhomogeneous distributions of NFs, the overall agreement between the various techniques is deemed reasonable. Indeed, the agreement is excellent for the OWL with larger and fewer NFs. The N and <d> values averaged over all three techniques are given in Table 4.17.

Table 4.17. Summary of the OW-alloy characteristics measured in this study

Alloy	OWH	OWI	OWL
O (wt.%)	0.249	0.127	0.065
N (wt.%)	0.190	0.013	0.016
d_l (μm)	9.4	11.3	23.3
d_s (μm)	0.151	0.582	0.323
f_s (%)	70	10	2
Technique			
TEM <d> (nm)	3.4	2.4	4.7
APT <d> (nm)	1.7	2.5	5.8
SANS <d> (nm)	2.8	2.8[a]	5.4
TEM N (10^{23} m^{-3})	1.2	2.8	0.6
APT N (10^{23} m^{-3})	2.9	9.6	0.7
SANS N (10^{23} m^{-3})	11	7.1[a]	0.5
SANS f (%)	1.2	0.8[a]	0.4
APT Y/Ti/O	22/37/41	11/42/47	22/31/46
Averages			
O (wt.%)	0.249	0.127	0.065
NF Av. <d> (nm)	2.6	2.6	5.3
NF Av. N ($10^{23}m^{-3}$)	5.0	6.5	0.6
Grain Av. <d_g> (μm)	2.9	10.2	22.8
μH (kg/mm^2)	443±12	368±4	252±7

[a] *equivalent milled and annealed powder*

The increase in H_v with O is due to variations in both NF hardening and the Hall-Petch grain size dependent strengthening contribution. The yield stress (σ_{ys}) can be empirically approximated as 2.5 Hv, as calibrated to the OWI alloy. The combined contributions of NF and Hall-Petch hardening can be approximated as

$$\sigma_{ys} = C_0 + C_1/\sqrt{\langle d_g \rangle} + C_2\sqrt{f}/\langle r \rangle$$

Here <d_g> is the area fraction weighted average of the small and large grain sizes, f is the volume fraction of the NF and <r> is their average radius. Using the SANS evaluation of f and <r> yields values of C_0 = 420 MPa, C_1 = 0.34 MPa-m$^{1/2}$ and C_2 = 6250 MPa-nm. Both C_1 and C_2 values are very reasonable and, notably, C_2 is consistent with a previous evaluation of NF hardening [7].

This study demonstrated the critical importance of the O content to achieving a high concentration of small NFs in a fully ferritic NFA. These results are broadly consistent with the effect of O observed in transformable 9Cr-ODS steels [25,29], albeit without the complication of a dual phase martensite-ferrite matrix. The higher hardness in OWH is in some part due to the larger fraction of fine grains in this case. Indeed, even though the intermediate O content OWI NFA had a higher concentration of NFs, it primarily manifests large grains, leading to a lower strength. Fits to the H_v and microstructural data yielded reasonable values of Hall-Petch and NF hardening coefficients. The large grains in the low O OWL alloy are likely due to fewer and larger NFs in this case. The difference in the grain structure in OWI and OWH are not understood and perhaps the higher N in OWH plays a role.

4.1.3 Mechanical testing

Only a limited amount of material property data was acquired since this study focused mainly on the character of the NFs. In addition, much of the work was performed on powders. Hardness measurements were made on all five of the consolidated alloys, and a limited number of creep and fracture measurements were also performed on the OW4 and PM2 alloys.

While the OW1 and OW2 alloys are generally similar, the pre-annealed OW2 alloy has a slightly lower hardness of 429±12 kg/mm^2 versus 443±14 kg/mm^2 for OW1. The lower number density of larger NFs in OW3 resulted in a low Vicker's hardness of 250±7 kg/mm^2. The OW4 alloy had a higher hardness of 368±4 kg/mm^2 than OW3 but lower than OW1 and OW2. The higher hardness in OW1 is in some part due to the smaller fraction of large grains in this case ($f_l \approx 30\%$). Indeed, even though the OW4 NFA had a

higher concentration of NFs, it primarily manifests large grains ($f_l \approx 90\%$), leading to a lower strength. Fits to the H_v and microstructural data yielded reasonable values of Hall-Petch and NF hardening coefficients. The large grains in the OW3 alloy are likely due to fewer and larger NFs in this case. The difference in the grain structure in OW1 and OW4 are not understood and perhaps the higher N in OW1 plays a role. A hardness of ≈ 401±15 kg/mm^2 was measured in PM2, although an increase in hardness up to ≈ 440 kg/mm^2 occurred within several mm distance from the can material likely do to C pickup.

The quantity of consolidated OW1 and OW2 material was not enough for mechanical testing and the structural analysis and hardness results of OW3 did not warrant further analysis. Larger quantities of OW4 and PM2 were available for tensile, creep, and fracture experiments. However, most of this ongoing work was carried out after the end date of the NERI grant so will be reported in the future in our new NEUP program.

4.2 A systematic study of the effects of Y and Ti variations

The matrix of 10 h SPEX milled powders, shown in Table 2.6, was produced with systematic variations in the Ti and Y_2O_3 content variations from a baseline composition of Fe-14Cr-3W-0.4Ti-0.3Y_2O_3. The milling procedure was described in section 2.2.

4.2.1 Oxygen and Nitrogen content

The O and Nitrogen content was measured in a subset of the 5 powders in the as-milled condition using the inert gas fusion method as shown in Table 4.18. The O and N are similar in 4 out of the 5 powders averaging 0.26±0.01 and 0.22 wt%, respectively. Much of this O and N was added as "impurities" during milling. Table 4.18 shows that the O and N content was dramatically reduced in the powder milled with an improved

can seal. Table 4.18 also shows excess O in terms of that over what is contained in the Y_2O_3. Therefore, the excess O and milling order is also given in Table 4.18.

Table 4.18. O and N comparison of select SPEX milled powders

Fe14Cr Alloy	Milling Order	Nitrogen (wt.%)	Oxygen (wt.%)	Excess O (wt.%)
0.40 Ti, 0.30 Y_2O_3 (no W)	1	0.264	0.265	0.204
0.20 Ti, 0.30 Y_2O_3	2	0.214	0.250	0.190
0.40 Ti, 0.40 Y_2O_3	3	0.200	0.258	0.168
0.33 Ti, 0.50 Y_2O_3	4	0.220	0.254	0.106
0.27 Ti, 0.40 Y_2O_3 (improved seal)	5	0.020	0.155	0.065

4.2.2 SANS

SANS measurements were carried out on all milled and annealed (1150ºC, 3 h) powder conditions. The SANS data in Figure 4.33 showed a systematic increase in f_v (Figure 4.33a) and N (Figure 4.33b) with increasing Y_2O_3. However, the effect of the Ti/Y ratio was much smaller except at the lowest Y_2O_3 and Ti/Y. The powder with 0.3 Y_2O_3 and a Ti/Y ratio of 1.6 is not shown because these results were highly inconsistent with the others, indicating a problem with the milling. This composition will be prepared and characterized again in the future.

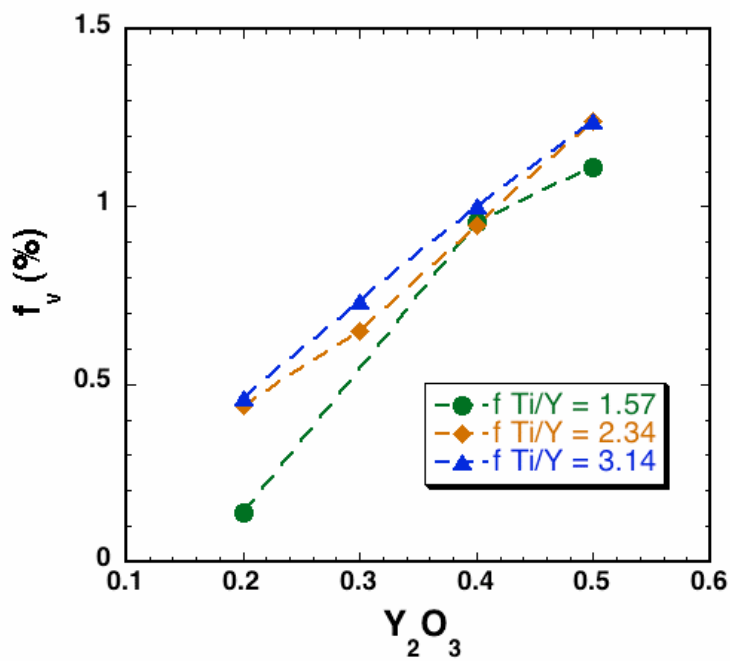

a)

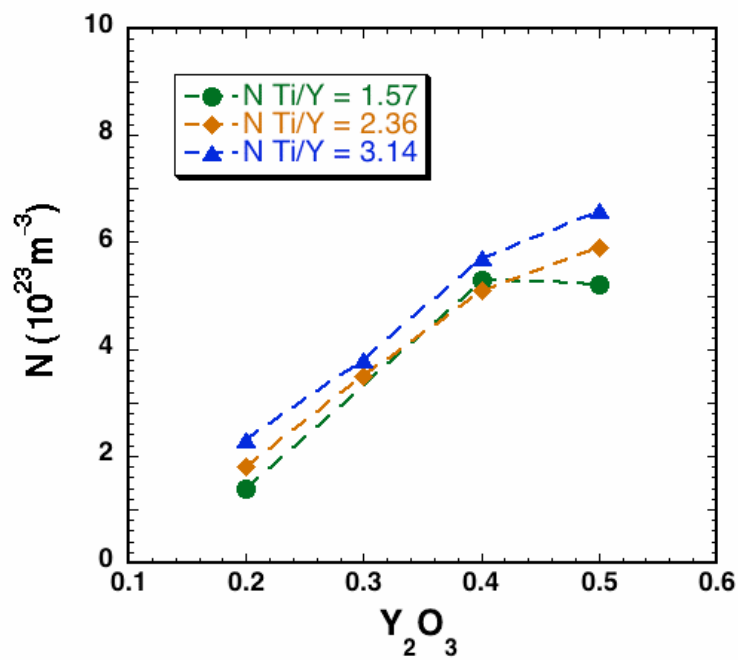

b)

Figure 4.33. a) Volume fraction (f_v) and b) Number density (N) versus Y_2O_3 for each Ti/Y ratio.

As shown in Figure 4.34, despite the large variation in Ti and Y_2O_3, the average size of the NFs was very similar for all alloys except for a slightly smaller value at the lowest Y_2O_3 and Ti/Y levels.

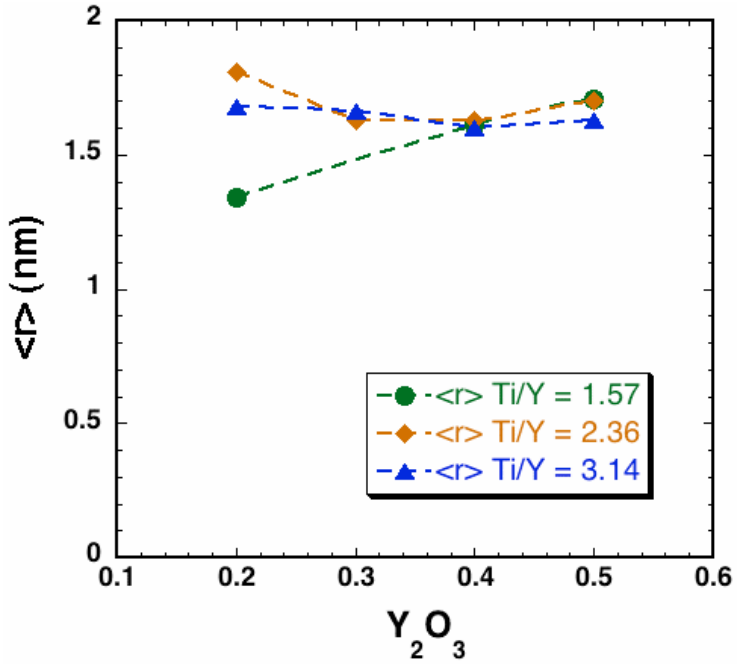

Figure 4.34. <r> versus Y_2O_3 for each Ti/Y ratio.

4.2.3 APT

APT was performed on 4 of the 12 milled and annealed powders. These APT measurements included all three Ti/Y ratios of powders with 0.3 wt.% Y_2O_3, as well as the powder milled with improved can sealing (0.4 wt.% Y_2O_3, Ti/Y = 1.6). The APT work is ongoing and was carried out after the end date of the NERI grant, and detailed results will be reported in the future in our new NEUP program. In summary the NF composition was virtually unchanged for each of the Ti/Y ratio powders as shown in Table 4.20. APT measured larger NF for the 0.3 Y_2O_3 and 1.6 Ti/Y ratio powder compared to the other powders, confirming the inconsistent SANS results for this same powder.

Table 4.19. NF composition comparison between powders with different Ti/Y ratios.

Powder	Y/Ti/O	Y/Ti	M/O
Ti/Y – 1.57, 0.4 Y_2O_3, 0.27 Ti	15.2/35.6/49.2	0.43	1.03
Ti/Y – 1.57, 0.3 Y_2O_3, 0.2 Ti	15.8/31.4/52.8	0.50	0.89
Ti/Y – 2.36, 0.3 Y_2O_3, 0.3 Ti	14.2/34.8/51.1	0.41	0.94
Ti/Y – 3.14, 0.3 Y_2O_3, 0.4 Ti	12.7/31.5/55.8	0.40	0.79

4.3 Friction stir welding

As previously shown, the microstructure of the MA957 FSW produced by the severe plastic deformation consists of a uniform distribution of fine scale equiaxed grains containing a high density of dislocations [26]. This differs from the microstructure observed in the as extruded (AE) base metal that is characterized by fine scale, textured grains elongated in the extrusion direction. Although some recovery of the grain dislocation substructure may occur, the average grain size in both the FSW and FSW and annealed (FSW-A) conditions is ~700 nm.

Five APT volumes were analyzed for the FSW, including two in the laser mode and three in the voltage mode, while four volumes were analyzed for the FSW-A condition in the voltage mode. Prior work included analysis of the AE condition, which is compared here to the FSW. The mass/charge spectra obtained by APT analysis exhibit numerous peaks from both elemental (Y, Fe, Cr, …) and molecular (FeO, YO, TiO, …) ions. The bulk compositions included trace levels of B, C, Al, Si, Mn, Ni, Co, Nb, V, P and Cu. The average bulk Ti compositions are about 0.85 at.% (AE), 0.76 at.% (FSW) and 0.38 at.% (FSW-A). The corresponding O concentrations are about 0.35 at.% (AE), 0.14 at.% (FSW) and 0.15 at.% (FSA-A). Very low levels of bulk Y (<0.02 at.%) were observed in both the FSW and FSW-A conditions, compared to an average of 0.08 at.% Y for the AE case. The higher Y content in the AE case is partly due to several APT samples

containing larger Ti-Y-O precipitates, resulting in higher overall Y content. The bulk depletion of Y, O and Ti, in part, may be due to the presence of larger Ti and Y enriched oxides, as well as a variety of other coarser phases (>5–10 nm), such as TiOx and C–N–Ti–Cr precipitates, which are not intercepted in the small APT volumes. The additional decrease in the Ti concentration in the FSW-A condition may be due to the further growth of these TiOx and C–N–Ti–Cr precipitates.

The low Y content measured by APT compared to a bulk measurement is a result of the non-uniform distribution of NFs and possibly some APT microscope artifacts. One possible artifact is the Y and YO ions are preferentially evaporated from the NFAs in rapid, spatially and time correlated sequences due to a lower evaporation potential of the NF atoms. In this case, some of the Y ions may not be counted during the detector dead time period. Another factor may be that the relative small primary Y^{3+} peak falls on the post-peak tails of dominant Fe^{2+} isotope peaks, making the Y mass–charge ranging and background subtraction more challenging and uncertain than for large, isolated, low background peaks.

Notably, in all conditions more than 90% of the Y that is detected is associated with the NFs. A qualitative conclusion is that the FSW alloy does not contain larger amounts of Y, Ti and O re-dissolved in the matrix compared to the AE condition, and it appears that post-FSW annealing may result in further partitioning of these elements to the coarser scale phases, rather than re-precipitation of small NFs.

Examples of the distributions of fine scale NFs in both FSW and FSW-A samples, as highlighted by isoconcentration surfaces, are shown in Figure 4.35. Figure 4.35a where the NFs are generally highly aligned along what appear to be sub-boundaries or

dislocations in the FSW condition. Note that NF ordering to this degree is not observed in the AE MA957. The insert for the larger feature in Figure 4.35a shows that the NFs are enriched with Y, Ti and O as well as with the O ions of these metallic species (see further discussion on NF compositions below). Figure 4.35b suggests that the concentration of the NFs is lower in the FSW-A condition. Although it is less distinct and involves fewer NFs in this case, there are also some indications of persistent NF alignment in the FSW-A condition. However, the highlighted boundary in the FSW-A volume, as shown in Figure 4.35b, does not contain NFs and is abutted by NF depleted zones. This may indicate that the boundaries and dislocations, which result in NF alignment in the FSW condition, migrate during the 1150°C–3 h annealing treatment. However, these data are too limited to reach firm general conclusions. This boundary in the FSW-A sample in Figure 4.35b is also marked by segregated Ti, Mo and Mn. The boundaries are also enriched in up to 18 and 20 at.% Cr in the FSW and FSW-A conditions respectively. Boron enrichment near a boundary is also observed in the FSW sample. The grain boundary segregation region width is about 1.5–2 nm. The most important and conclusive observation that can be deduced from these results is that the NFs persist following FSW. However, the NFs appear to be altered and redistributed during severe deformation and some dissolve during post-FSW annealing.

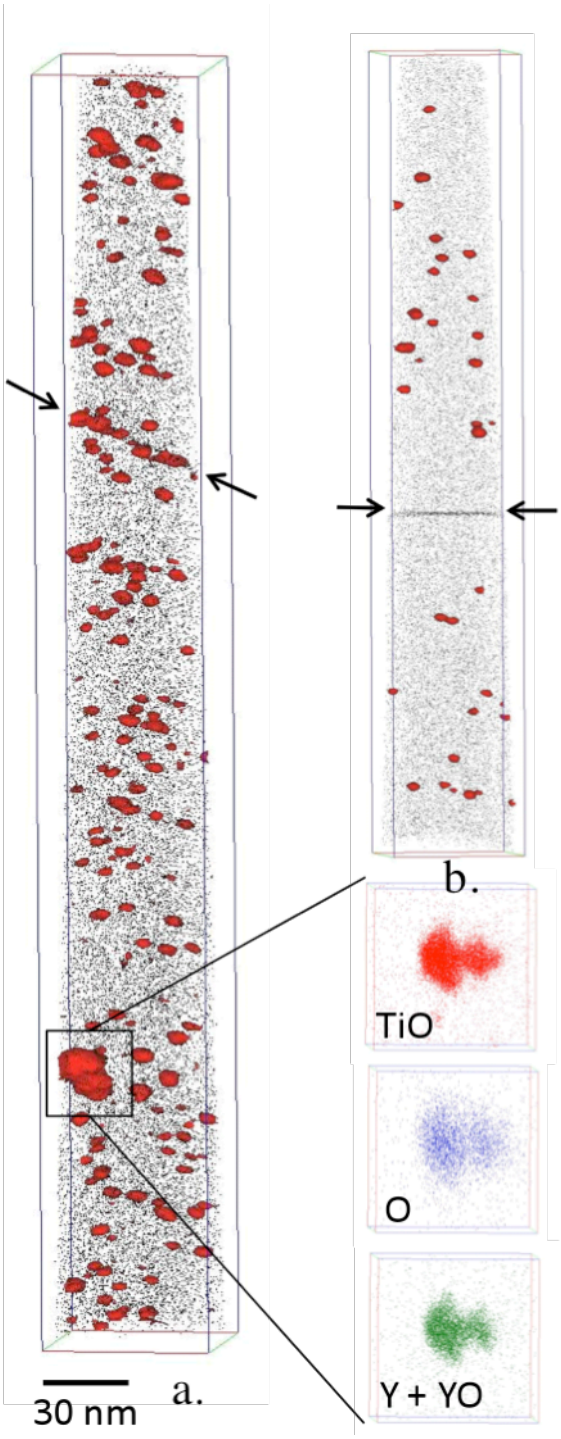

Figure 4.35. a) An APT 3-D reconstruction of a volume of the FSW MA957 showing the isoconcentration surfaces (1 at.% TiO and YO) to identify the NFs. Arrows indicate a boundary. A blow-up of the TiO, YO+Y and O atoms for a larger feature is also shown; b) FSW-A sample with lower number density of NFs.

A summary of the measured diameter and number density results are shown in Table 4.20. The corresponding results for SANS and TEM characterization are also shown for comparison. In the APT data obtained in the present study, FSW apparently has minor effect on the NF N compared to the AE condition (about 3.2×10^{23} m^{-3} {AE} versus 1.6×10^{23} m^{-3}) and d (about 2.5 nm {AE} versus 2.2 nm). A decrease in N is consistent with the slightly lower hardness observed in the FSW versus the AE condition; 304 DPH (kg mm^{-2}) compared to 336 DPH. A few larger NFs of about 5–6 nm are observed in the FSW. Post-FSW annealing appears to reduce N (~0.9×10^{23} m^{-3}), but has little effect on the average d ≈ 2.2 nm. The decrease in N, perhaps combined with some substructure recovery, is consistent with hardness that is 11% lower in the FSW-A at ~270 DPH. The size distributions of the NFs in the FSW and FSW-A conditions are shown in Figure 4.36.

Table 4.20. Number density and average diameter of NFs in the MA957 FSW before and after annealing and in the AE metal.

NF d and N	Technique	AE	FSW	FSW-A
d (nm)	TEM	2.1 [27]	2.9	3.0
	APT	2.4	2.2	2.2
	SANS	2.7	2.5	-
N ($10^{23}/m^{-3}$)	TEM	4.5 [27]	1.1	1.1
	APT	3.2	1.6	0.9
	SANS	9.0	3.5	-

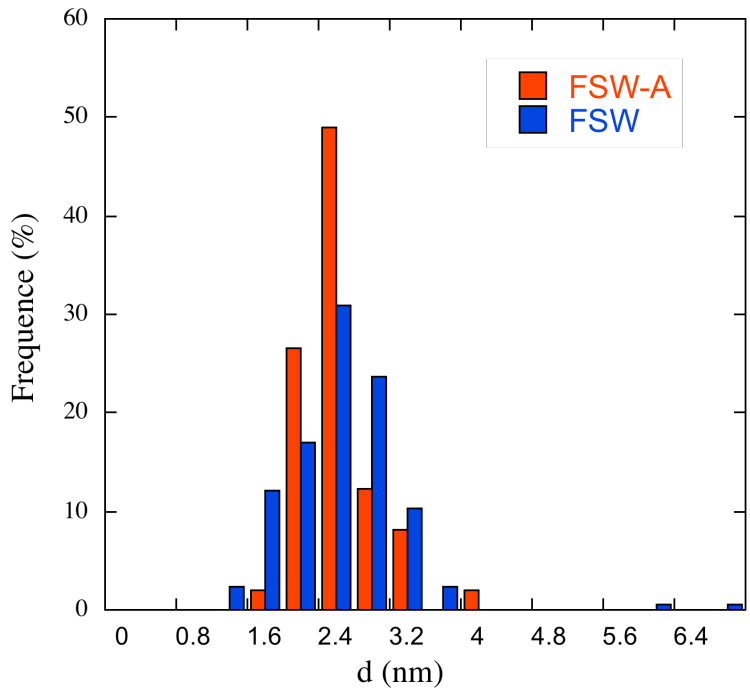

Figure 4.36. The APT NF size distributions for the FSW and FSW-A MA957.

The APT d values are smaller than those measured by TEM and SANS. The APT N values are also lower compared to the SANS data in all the AE and FSW conditions, as well as the TEM data for the AE specimens. However, the APT N values are larger than those measured by TEM for the FSW condition and are similar for the FSW-A case. The most notable difference is that the other techniques suggest that FSW decreases N more than that found in the APT measurements.

The inserts in Figure 4.35a suggest that the distribution of O atoms is broader than for Y, YO and TiO. This is also observed in AE MA957 and has been reported in several other APT studies of similar alloys [18,19]. The NFs are enriched in Y, Ti, O and with minor enrichment in Al. it is convenient to represent the NF compositions as Y/Ti/O percentages (i.e. excluding the matrix elements and neglecting minor constituents like Al). The differences in compositions for the three alloy conditions are minimal: 13.8/43.7/42.3 (AE), 14.8/40.3/44.9 (FSW) and 13.6/39.6/46.8 (FSW-A). Note that these

compositions do not correspond to any known stoichiometric Y–Ti–O phase, such as $Y_2Ti_2O_7$ and Y_2TiO_5.

TEM energy dispersive X-ray and diffraction data on extraction replica samples indicate that the small NFs are likely $Y_2Ti_2O_7$ pyrochlore complex oxides that contain no Fe and little or no Cr. EDX measurements have shown that the smallest (<5 nm) phases have typical Y/Ti/O fractions of 16/16/68, which are very close to the stoichiometric values for pyrochlore of 18.2/18.2/63.6. The micrograph in Figure 4.37 for the FSW-A condition shows that these oxides are truncated cube shaped polyhedra. Thus, the low value of Y/Ti from the APT measurements may be another artifact. As noted previously, this could be due to the effects of multiple hits of Y rapidly evaporated from the NFs.

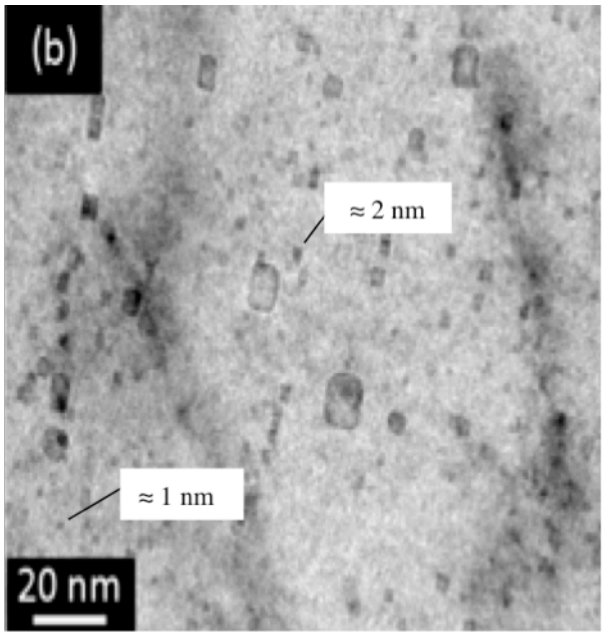

Figure 4.37. A bright field TEM image of crystalline $Y_2Ti_20_7$ oxides in the FSW-A down to approximately 1 nm.

5.0 Summary and Conclusions

The focus of this research was characterization of the powders and alloys through each processing step: powder production by gas atomization; powder milling; and powder hot consolidation by hot isostatic pressing or hot extrusion. The bulk chemistry measurements show that preliminary batches of gas-atomized powders could be produced within specified composition ranges. However, in the as-atomized condition the Y is phase separated and significant ball milling is required to adequately mix the alloy. This is unfortunate as one goal of the study was to explore ways of reducing or eliminating ball milling.

TEM, SANS and APT show that SPEX milling for 10 h or attritor milling for 20 to 40 h sufficiently mixes the Y. Notably, effective mixing does not occur at lower milling times, and the powder atomized in the Ar/O atmosphere may require more milling than the Ar atomized powder. No Y-Ti-O precipitates are present after milling, but the solutes are concentrated on dislocation cell or grain boundaries, but not highly associated with each other. Additional work is required to determine the differences between the Ar and He powder, but the Y distribution, measured by EPMA, was slightly more uniform in the He case. The bulk of this work was performed on Ar atomized powder material after obtaining the preliminary results.

Initial milling procedures in this study added a significant quantity of O as well as contaminant N. Modifying the attritor mill chamber evacuation and backfill procedure effectively eliminated the N contamination but also reduced the O content. Oxygen was added to the final alloys examined by milling the atomized powders with FeO. TEM, SANS and APT show that subsequent powder annealing treatments or HIP consolidation,

typically at 1150°C, result in a bimodal grain structure with a uniform, high density of NFs precipitating in both the large and small grains. Larger Ti-nitride and Ti-oxide precipitates formed in alloys with high N and O contamination. Alloys extruded at a lower temperature of 850°C contained a unimodal distribution of fine grains.

The effects of annealing or consolidation temperature were briefly explored. A set of L2311M powder after milling for 40 h with FeO was annealed at 850ºC, 1000ºC, and 1150ºC in ramp anneal and iso-thermal annealed conditions. The lowest temperature anneal at 850ºC contained the smallest NFs with the highest number density and volume fraction. The NF size systematically increased and the number density and volume fraction decreased with annealing temperature. Iso-thermal annealing tends to produce slightly smaller NFs as seen in the L2311M powder milled with FeO and the OW2 HIP alloy that was isothermally annealed at 1000ºC before consolidation.

Four HIP alloys consolidated at 1150ºC include OW1, OW2, OW3, and OW4. The final alloy, PM2, was extruded at 850ºC and annealed for 1 h at 1000ºC before being cross-rolled to 50% thickness. A comparison between OW1, OW3, and OW4 showed the effects high, low, and medium amounts of O have on the NFs. Low O content produced fewer and coarser NFs, with higher Y/Ti ratios and a larger average grain size compared to the medium and high O content NFAs. TEM showed the low O alloy (OW3) had NFs with Y/Ti ratios much greater than 1. However, APT showed the ratio was less than 1 but gave a higher Y/Ti ratio compared to OW1 and OW4. The APT measured Y/Ti/O ratios for the OW1, OW3, and OW4 alloys were 22/37/41, 22/31/46, 11/42/47, respectively. Alloys with low, medium and high O content had microhardness values of 252±7, 368±4, and 443±12 kg/mm^2, respectively. The difference in hardness between the medium and

high O alloys may partially be attributed to the bimodal grain size distribution, with the high O alloy having a greater fraction of small grains (< 1 μm) compared to the medium O alloy. The PM2 alloy's hardness was 401±15 and the Y/Ti/O ratio was 11/44/45. A summary of the microhardness and NF <d> and N for most of the consolidated alloys is given in Table 5.1.

Table 5.1. Summary of the consolidated alloy characteristics measured in this study

Alloy	**OW1**	**OW4**	**OW3**	**PM2**
O (wt.%)	0.249	0.127	0.065	-
N (wt.%)	0.210	0.013	0.016	-
Technique				
TEM <d> (nm)	3.4	2.4	4.7	1.4
APT <d> (nm)	1.7	2.5	5.8	2.1
SANS <d> (nm)	2.8	2.8[a]	5.4	-
Average <d> (nm)	**2.6**	**2.6**	**5.3**	**1.8**
TEM N (10^{23} m^{-3})	1.2	2.8	0.6	5.8
APT N (10^{23} m^{-3})	2.9	9.6	0.7	11.0
SANS N (10^{23} m^{-3})	11	7.1[a]	0.5	-
Average N (10^{23} m^{-3})	**5.0**	**6.5**	**0.6**	**8.4**
SANS f_v (%)	1.2	0.8[a]	0.4	-
APT Y/Ti/O	22/37/41	11/42/47	22/31/46	11/44/45
μH (kg/mm^2)	443±12	368±4	252±7	401±15

The effects Ti and Y content on the NFs in annealed powders that were conventionally milled with 3 concentrations of Y_2O_3 ranging from 0.2 to 0.5 wt.% at 3 Ti/Y ratios of 1.6, 2.4, and 3.1 (12 nominal conditions although one milling run failed). SANS measurements showed that the NF N and f_v increase in proportion the Y_2O_3 but generally are only weakly dependent on the Ti/Y ratio. Further the <r> are insensitive to the powder composition. APT showed that the variation in bulk Y and Ti had little effect on the NF composition.

APT characterization of a MA957 friction stir weld showed that this solid sate joining procedure had only a modest effect on the NF N and <d>. Annealing at 1150ºC for 3 h following FSW reduces N, consistent with a significant reduction in hardness. FSW appears to rearrange the NFs, which become highly aligned with sub-boundary and dislocation structures to an extent that are not observed in the as extruded case. The aligned NF structures are less apparent, but seem to persist after annealing. The size and number densities measured in APT are of the same order as those measured in TEM, but, on average, are lower. The N values measured in SANS studies are higher. This may be due to both detectability and sampling volume limits of APT and resolution limit for TEM that result in the failure to detect some of the smallest NFs.

Several NFA materials, including MA957 and various 14YWT alloys, have been included in irradiation experiments. These experiments have been performed or are currently in play at numerous facilities including the Advanced Test Reactor (ATR), the JOYO sodium cooled fast reactor, the High Flux Isotope Reactor (HFIR), and the SINQ spallation neutron source for the SINQ Target Irradiation Program (STIP).

Acknowledgments

Support for this research was primarily provided by the U.S. Department of Energy (DOE) Office of Nuclear Energy through the Nuclear Energy Research Initiative Program (DE-FC07-07ID14825). Additional support for some aspects of this research was provided by the DOE Office of Fusion Energy Sciences and the DOE Office of Nuclear Energy Fuel Cycle R&D Program in a collaboration led by Los Alamos National Laboratory (LANL). We also acknowledge the support of the National Institute of Standards and Technology Center for Neutron Research in providing the neutron scattering facilities used in this work. Support at UCSB included the NSF Materials Research Laboratory microscopy and microanalysis facility and the Materials Processing Laboratory. We also would like to acknowledge our research partners, including LANL, University of California Berkeley (UCB), Oak Ridge National Laboratory (ORNL), South Dakota School of Mines (SDSM) and ATI Powder Metals, with special thanks to Stuart Maloy at LANL and David Hoelzer at ORNL.

REFERENCES

1. G.R. Odette, M.J. Alinger, and B.D. Wirth, Annual Review of Materials Research, Vol. 38, (2008) 472.

2. G.R. Odette and D.T. Hoelzer, *J. of Mat.*, 62-9 (2010) 84.

3. Luvak Inc., 722 Main Street, Boylston, MA, 01505.

4. Harris, A.M., Schaffer, G.B., and Page, N.W., "A novel technique for the preparation of metal powders for transmission electron microscopy", *J. of Mat. Sci. Letters*, 12, 1993, 160-161.

5. Buehler Ltd., 41 Waukegan Road, Lake Bluff, IL, 60044.

6. Leco Corporation, 3000 Lakeview Avenue, St. Joseph, MI, 49085.

7. Alinger, M.J., September 2004, *On the Formation and Stability of Nanometer Scale Precipitates in Ferritic Alloys during Processing and High Temperature Service*, Thesis (PhD), University of California Santa Barbara.

8. Ohtsuka, S., Ukai, S., Fujiwara, M., Kaito, and Narita, T., *J. of Physics and Chemistry*, 66, 2005, 571-575.

9. Glinka, C.J., Barker, J.G., Hammouda, B., Krueger, S., Moyer, J.J., and Orts, W.J., J. *Appl. Cryst.*, 31, 1998, 430.

10. M.J. Alinger, G.R. Odette, and D.T. Hoelzer, *Acta Mater*, 57 (2009) 392.

11. Mader, E., 1995, *Kinetics of irradiation embrittlement and post-irradiation annealing of nuclear reactor pressure vessel steels*, Thesis (Ph.D), University of California, Santa Barbara.

12. M. K. Miller, *Atom Probe Tomography: Analysis at the Atomic Level*, Kluwer Academic/Plenum Publishers, New York (2000).

13. K. Thompson, D. Lawrence, D.J. Larson, J.D. Olson, Kelly, T.F., and B. Gorman, *Ultramicroscopy*, 107, 2007, 131.

14. E. Oltman, R.M. Ulfig, and D.J. Larson, *Microscopy and Microanalysis*, 15 Supplement 2, 2009, 256-257.

15. D. Vaumousse, A.Cerezo, P.J. Warren, *Ultramicroscopy,* 95, 2003, 215.

16. J.M. Hyde, C.A. English, in: G.E. Lucas, M.A. Kirk Jr, R.G. Elliman (Eds.), Proc. of the MRS 2000 Fall Meeting, Symp. R: Microstructural Processes in Irradiated Materials 650, Materials Research Society (2000/2001) R6.6.1.

17. R.P. Kolli and D.N. Seidman, *Microsc. Microanal.*, 13, 2007, 272.

18. C.A. Williams, E.A. Marquis, A. Cerezo, G.D.W. Smith, *J. Nuclear. Mat.,* 400, 2010, 37.

19. E.A. Marquis, *Appl. Phys. Lett.*, 93, 2008, 181904

20. E.A. Marquis, F. Vurpillot, *Microsc. Microanal.* 14, 2008, 561.

21. Hamilton, M.I., Gelles, D.S., Lobsinger, R.J., Johnson, G.D., Brown, W.F., Paxton, M.M., Puigh, R.J., Eiholzer, C.R., Martinez, C. and Blotter, M.A., "Fabrication technological development of the oxide dispersion strengthened alloy MA957 for fast reactor applications", Technical Report PNL-13168, 1991, Richland, WA: Pacific Northwest Lab.

22. Wu, Y., Haney, E., Cunningham, N., and Odette, G.R., Submitted to *Acta Materialia*, 2011.

23. Eiselt, C., Klimenkov, M., Lindau, R., and Moslang, A., *J. Nuclear Mat.*, 386-388, 2009, 525-528.

24. Etienne, A, Cunningham, N.J., Wu, Y., and G.R. Odette, *Mat. Science and Tech.*, Vol. 27, 2011, 724-728.

25. Ukai, S. and Ohtsuka, S., *Energy Materials*, Vol 2, 2007, 26-35.

26. Miao, P., Odette, G.R., Gould, J., Bernath, J., Miller, R., Alinger, M., and Zanis, C., *J. of Nuclear Mat.*, 367-370, 2007, 1197-1202.

27. Miao, P., Odette, G.R., Yamamoto, T., Alinger, M.J. and Klingensmith, D., *J. Nuclear Mat.*, 377, 2008, 59-64.

28. Ohtsuka, S., Ukai, S., Fujiwara, M., Kaito, T., Narita, T., *J. Nuclear Mat.,* 329:372, 2004.

29. Ohtsuka, S., Ukai, S., Fujiwara, M., Kaito, T., Narita, T., *J. Phys Chem of Solids,* 66:571, 2005.